International Journal of Extreme Manufacturing

Interpretable machine learning integrated with physicochemical feature for developing additively manufactured ultra-high strength and ductility steel

OPEN ACCESS
IMMT | IOP Publishing
International Journal of Extreme Manufacturing
Int. J. Extrem. Manuf. **8** (2026) 045001 (23pp)
https://doi.org/10.1088/2631-7990/ae5006

Interpretable machine learning integrated with physicochemical feature for developing additively manufactured ultra-high strength and ductility steel

Yating Luo[1], Tao Zhu[2], Cunliang Pan[1], Xu Ben[1], Xudong An[1], Xiaoming Wang[3] and Hongmei Zhu[1,*]

[1] Key Laboratory of Hunan Province of Equipment Safety Service Technology under Extreme Environment, University of South China, Hengyang 421001, People's Republic of China
[2] School of Computer, University of South China, Hengyang 421001, People's Republic of China
[3] School of Engineering Technology, Purdue University, West Lafayette, IN 47907, United States of America

E-mail: meizihong999@126.com

Received 19 September 2025, revised 4 December 2025
Accepted for publication 9 March 2026
Published 31 March 2026

Abstract

The multi-component complexity of ultra-high strength and ductility steels (UHSDS) imposes significant challenges for physical metallurgy-guided machine learning (ML) and CALPHAD-combined ML optimization design. Currently, the reported additively manufactured UHSDS necessitate multi-step heat treatments and expensive alloying elements while exhibiting poor corrosion resistance. In this study, a physicochemical feature-integrated, interpretable ML strategy was employed to design multi-component UHSDS fabricated via laser-directed energy deposition (LDED). SHapley additive exPlanation (SHAP) analysis was performed to reveal the critical intrinsic factors and their effects on the tensile mechanical performance, including ultimate tensile strength (UTS), yield strength (YS), and elongation (EL). Accordingly, the candidate alloying elements were identified, and a simple single-step tempering heat treatment was adopted, enabling the synchronous enhancement of strength and ductility. As a consequence, we designed a novel cost-effective and short-process LDEDed Fe-15Cr-3.2Ni-0.8Mn-0.6Cu-0.56Si-0.4Al-0.16C UHSDS, followed by tempering at 480 °C for 6 h. The as-tempered specimen mainly consisted of lath martensite, together with some austenite, carbides and nano-precipitates (AlN, NiAl, and ε-Cu). Both striking mechanical properties (i.e., UTS: (1 713 ± 17) MPa, YS: (1 502 ± 33) MPa, EL: (15.5 ± 0.7)%) and excellent corrosion resistance, with a corrosion rate of 0.105 mm·a^{-1}, have been achieved,

* Author to whom any correspondence should be addressed.

superior to the reported additively manufactured UHSDS. The ultra-high strength and ductility are attributed to solid–solution strengthening, precipitate strengthening and transformation-induced plasticity (TRIP) effects. This work will be of great significance to provide new insights into the development of low-cost and process-simplified UHSDS, especially for the laser fabrication of high-value-added steel components with excellent comprehensive performance.

Keywords: additive manufacture, machine learning, physicochemical feature, cost-effective and short process, ultra-high strength and ductility steel, corrosion resistance

Supplementary material for this article is available online

1. Introduction

Additively manufactured ultra-high strength and ductility steel (UHSDS), owing to its exceptional mechanical properties, has demonstrated vital applicability in strategic sectors, including aerospace, automotive manufacturing, and marine transportation[1–4]. However, many engineering applications have been severely restricted because of the high-content expensive alloying elements such as Ni, Mo or Co[5–7] and the required complex heat treatment (including solutionizing at 800–1 200 °C, followed by quenching at 950–1 050 °C and 2–3 times tempering at 270–350 °C)[6–9].

To date, the applications of machine learning (ML) in additive manufacturing have spanned material design[10–20], process optimization[21,22], and structural design[23,24]. Specifically, the ML method has opened new avenues for material design, which enables the construction of data-driven models that can rapidly elucidate the complex structure−property relationships inherent in material systems[10]. Currently, ML facilitates the optimization of high-performance steel compositions and processing parameters by using the two following modeling methods: composition-processing-properties (CPPs) and composition-processing-intermediate variables-properties (CPPPs). However, the CPP-ML model relies on the explicit mapping relationships among composition, processing parameters, and properties, imposing high demands on dataset quality[11]. The CPIP-ML model incorporates intermediate variables to mitigate data scarcity limitations for material design optimization. These intermediate variables are derived in the following three ways[12–20]: physical metallurgy (PM) models[12–14], CALPHAD[15,16], and physicochemical feature (PF) screening[18–20].

For the ML optimization design strategy integrated with PM (PM-ML), Shen et al.[12] designed a cast Fe-13Cr-1.54Ni-13Co-5.3Mo-0.004C ultra-high strength stainless steel followed by a multi-step heat treatment, including 1 050 °C × 1 h solutionization, 5 h cryogenic treatment in liquid nitrogen, and 560 °C × 4 h tempering treatment. The equilibrium volume fraction (V_f) and thermodynamic driving force (D_f) served as key intermediate variables. However, their modeling lacked the prediction of mechanical properties except hardness and neglected the retained austenite. Similarly, He et al.[13] designed a hot-rolled Fe-2.5Cr-0.3Cu-0.1Ni-0.13Ti-0.05C weathering steel by employing phase transformation critical points (A_{c1}, A_{c3}), a carbon equivalent (C_{eg}) and the atmospheric corrosion resistance index (I) as intermediate variables. Nevertheless, the model failed to account for dynamic phase transformation phenomena, particularly the formation of non-equilibrium bainite/martensite during the rolling process. Cui et al.[14] improved the prediction accuracy of YS and EL for a hot-rolled Fe-1.35Mn-0.24Cr-0.12Ti-0.15Si-0.05Al-0.0769C steel, by reconstructing rolling parameters into microstructural descriptors as intermediate variables, namely, the dislocation density, fraction and size of the TiC precipitate and ferrite. However, the time scale of strain-induced TiC precipitation was not fully incorporated, leading to deviations in the prediction of precipitate size. Although the PM-ML strategy demonstrates improved prediction capability by simplifying PM principles, this methodology fails to account for dynamic multi-physics interactions (i.e., temperature−strain−time coupling) during actual processing and results in quantifiable systematic errors.

For the CALPHAD-informed ML (CALPHAD-ML) methodology, intermediate variables are integrated to derive thermodynamic domain knowledge constraints. Tan et al.[15] designed an additively manufactured Fe-20.8Ni-6.2Ti-1.7Al martensitic steel by employing CALPHAD to obtain intermediate variables that drive ML models for predicting phase content. Critical phase constraints (Max Ni_3Ti, Laves < 5 wt%) were established through coupled thermodynamic equilibrium analysis, precipitation kinetics, and microstructural stability assessment. Similarly, Li et al.[16] designed two cast reduced-activation ferritic/martensitic (RAFM) steels (Fe-8.6Cr-1.3W-0.3Si-0.57Mn-0.32V-0.18Ta-0.14C and Fe-8.4Cr-0.26W-0.15Si-0.50Mn-0.31V-0.17Ta-0.055C) by incorporating restrictions (i.e., without δ-ferrite at the normalizing temperature (NT); without coarsening phases at the tempering temperature (TT); V_{MX} 0.4% at TT; $V_{M23C6} \leq 1.5\%$ at TT). Nevertheless, the CALPHAD-ML approach suffers from several inherent limitations: (i) strong reliance on empirical thermodynamic constraints, requiring extensive thermodynamic data; (ii) substantial computational complexity due to high compositional dimensionality, leading to significantly increased cost and reduced accuracy.

The PF-integrated machine learning (PF-ML) paradigm couples interpretable material descriptors with data-driven modeling frameworks systematically[17]. Table 1 presents a comparison of the PM-ML, CALPHAD-ML and PF-ML approaches. Obviously, the PF-ML methodology offers distinct advantages over the other two methods. Specifically, it can overcome the heavy reliance on empirically derived parameters and simplified assumptions in PM-ML, which

Table 1. Comparison of CALPHAD-ML, PM-ML and PF-ML approaches[12–20].

Characteristic \ Approach	CALPHAD-ML	PM-ML	PF-ML
Data efficiency	Medium	Medium	High
Extrapolation capability	Low	Low	High
Interpretability	Medium	High	High
Model complexity	Medium	High	Medium
Computational cost	High	Medium	Low

often leads to poor extrapolation performance. Meanwhile, the PF-ML addresses the strong dependency on the limited thermodynamic databases, triggering large uncertainties in high-dimensional composition spaces for CALPHAD-ML. Therefore, PF-ML is characterized by superior data efficiency, robust mechanism-aware extrapolation, improved interpretability, and lower computational costs.

Currently, the PF-ML approach has been effectively utilized in the development of advanced materials, including copper alloys with high conductivity[18], aluminum alloys with high stress-corrosion resistance[19] and high entropy alloys with high hardness[20]. For instance, Zhang et al.[18] designed four Cu-In alloys (Cu-0.68In, Cu-0.42In, Cu-0.26In and Cu-0.30Sn-0.27In) by incorporating key physicochemical features, including E4 (absolute electronegativity), S6 (core electron distance) for UTS, and S10 (atomic radius) for electrical conductivity (EC). Notably, the generalizability of this methodology was further validated in aluminum alloy systems, where the identical set of descriptors (E4, S6, and S10) maintained robust predictive capability. Likewise, Jiang et al.[19] developed an Al-10.50Zn-2.31Mg-1.56Cu-0.09Ti-0.15Cr-0.10Zr alloy by integrating physicochemical features, including G4-1 (d-orbital electron count), C2-1 (boiling point), S6-1 (nuclear−electron distance) and S14-2 (acoustic velocity variance) for UTS; S16-1 (density), E5-2 (variance in first ionization energy) and E13-1 (electrical resistivity) for fracture ductile (KIC); C14-1 (diffusion activation energy), E15-1 (corrosion potential) and C20-1 (Young's modulus) for stress corrosion resistance (ISSRT). The PF-ML approach has been demonstrated to be an effective methodology; however, its application in the optimization design of high-performance steel has rarely been reported to the best knowledge of authors.

To address these challenges caused by factors such as the alloying element and the complex heat treatment (HT) parameter, we applied the PF-ML strategy for developing cost-effective and short-process UHSDS in this work. First, the key features affecting the UTS, YS, and EL were determined via feature screening. Subsequently, the interpretable Shapley additive explanation (SHAP) algorithm rooted in game theory[25] was employed to uncover the explicit laws of elements affecting properties. After the analysis results and evaluation criteria were combined, the alloying elements that can improve both the strength and ductility were determined. Finally, NSGA-III was leveraged for multi-objective optimization of the element contents and heat treatment parameters, then a novel cost-effective UHSDS with a simple single-step tempering treatment was designed. The synergistic mechanism for the concurrent improvement in the strength−ductility balance and corrosion resistance in the newly developed UHSDS was comprehensively revealed via experimental validation. This study aimed to achieve cost reduction, procedure simplification, and comprehensive performance enhancement, providing a new strategy for additively manufactured UHSDS via PF-ML methodology.

2. Design strategy

Figure 1 illustrates the PF-ML methodology for the UHSDS design framework, which consists of the following five steps: (i) initial dataset creation, (ii) feature screening and modeling, (iii) SHAP analysis, (iv) multi-objective optimization, and (v) experimental validation.

First, experimental data, including UTS, YS, EL and heat treatment parameters of UHSDSs, together with the physicochemical parameters of alloying elements for constructing alloy factors, were collected from both published literature and authoritative databases. As a consequence, experimental samples and element physicochemical characteristic quantity datasets were established for ML. Second, the key alloy factors were screened to set up models for UTS, YS, and EL via combining importance ranking with correlation screening and exhaustive calculations. Third, the SHAP analysis method was used to elucidate the specific influence of key physicochemical features on the UTS, YS, and EL. Furthermore, this analysis allows for the examination and ranking of potential elements, enabling the identification of candidate elements that can enhance both strength and ductility. Fourth, NSGA-III was applied to determine the optimal alloying element contents and heat treatment parameters. Finally, experimental verification was conducted to elucidate the mechanism underlying the simultaneous performance enhancement.

2.1. Dataset

A curated dataset was constructed by systematically collecting data on the composition and heat treatment process parameters of high-strength steels fabricated via laser-based additive manufacturing techniques, specifically, laser powder bed fusion (LPBF) and laser directed energy deposition (LDED), from published literature, including the Web of Science and China National Knowledge Infrastructure (CNKI). After screening under the constraint conditions of UTS $\geq$ 1 200 MPa and YS $\geq$ 1 000 MPa, a dataset with 106 sets of data was built, with a focus on three key mechanical properties including UTS, YS, and EL (see Supplementary Material 1). The interquartile range (IQR) method was used to identify outliers with data point exceeding Q1 $-$ 1.5 $\times$ IQR and Q3 $+$ 1.5 $\times$ IQR for a given property, which were rigorously excluded to ensure data reliability and reduce experimental bias[26]. The

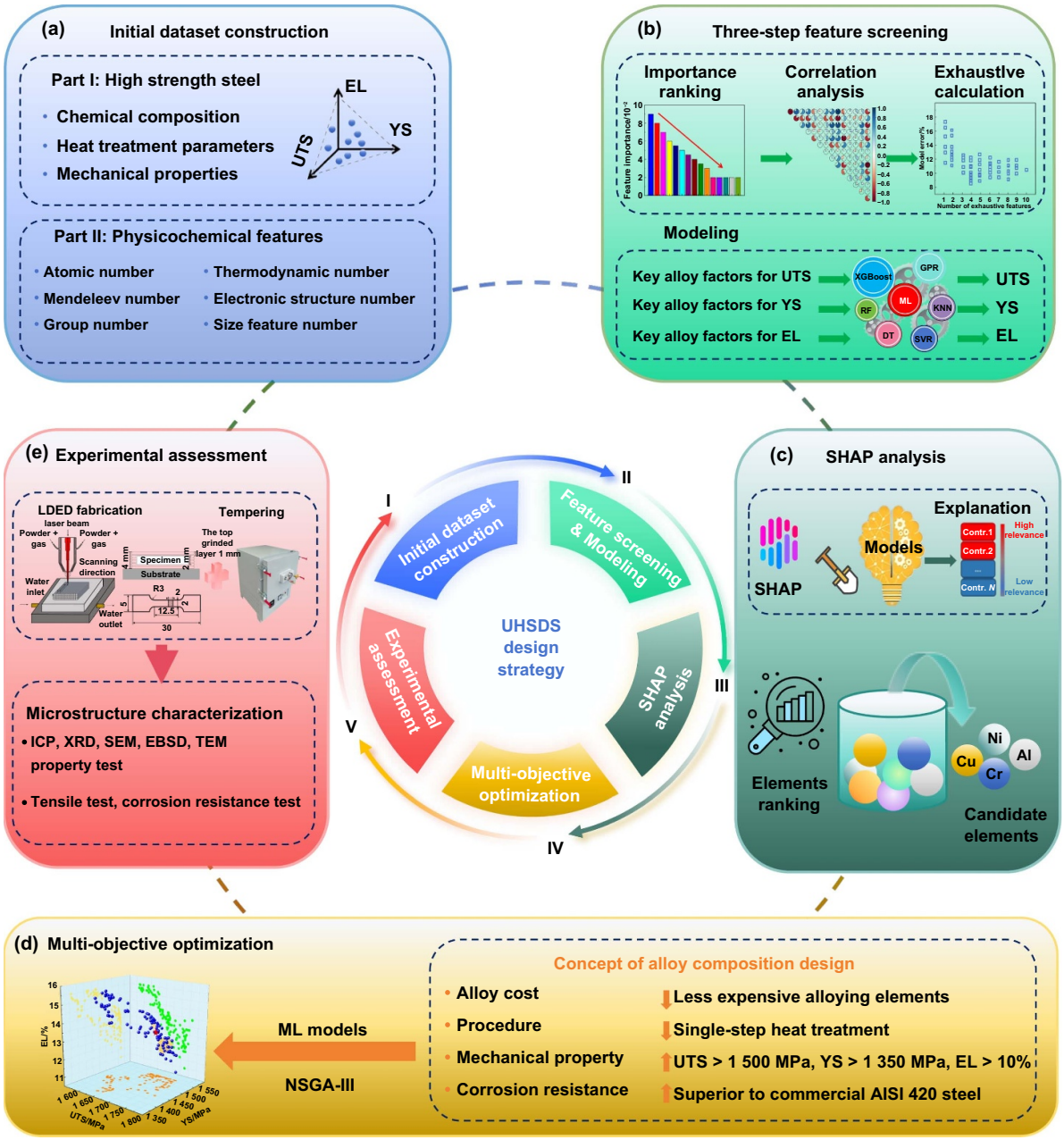

Figure 1. The PF-ML design strategy for cost-effective, short-process, and corrosion resistant UHSDS: (a) initial dataset construction,(b) feature screening and modeling, (c) SHAP analysis, (d) multi-objective optimization, (e) experimental assessment.

above data collection approaches can effectively minimize the interference of process parameters in performance predictions.

2.2. Features

Quantitative analysis of the composition-property correlations has been persistent challenges in materials science[27]. To eliminate the impact of additive manufacturing methods (i.e., LPBF and LDED) on mechanical property variability, physicochemical features are introduced in this work to serve as the primary inputs of the ML models, which can dictate the alloy's response to the thermo-kinetic conditions of different laser fabrication processes[28]. By connecting input features with physical mechanisms, the statistical correlations can be transformed into actionable design guidelines. This process is termed as "feature interpretation", which can explain the ML predictions well[29]. Based on the alloy factor establishment method developed by Zhang et al.[18], 81 physicochemical features were extracted for each element, such as atomic number, group number, Mendeleev number, thermodynamic number, electronic structure number and size, which were classified into 6 categories in this work, see Supplementary Material 2. Specifically, the mean factor f_{mi} and the variance factor f_{vi} for the 81 feature quantities were calculated via Equations (1) and (2), respectively, which are termed as alloy factors and provide a comprehensive representation of the characteristics of the studied samples.

$$f_{mi} = \sum (f_{ij} \times \alpha_j) / \sum \alpha_j \quad (1)$$

$$f_{vi} = \sum (f_{ij} - f_{mi})^2 \times \alpha_j / \sum \alpha_j. \quad (2)$$

Where f_{ij} denotes the feature quantity associated with the individual element, i is the different feature quantity of each element (i= 1, 2, 81), j corresponds to the different elements present within the sample alloy ($j = 1, 2\ldots, n$, n is the number of alloy compositions), and α_j represents the atomic percentage content of element j.

Herein, a three-step feature screening method based on extreme gradient boosting (XGBoost) was applied to screen the key alloy factors as follows:

Step I: importance ranking. Considering the small sample size and high-dimensional feature of this study, the XGBoost algorithm[30] was utilized to quantify and prioritize the contribution weights of the alloy factor. For the trained XGBoost models, the importance of the input variables (162 constructed alloy factors) was determined by analyzing their frequency as segmentation nodes and their corresponding node weights. A weighted importance index was then calculated for each variable to establish the final ranking.

Step II: correlation analysis. Specifically, the Pearson correlation coefficient r[31] was calculated for any two alloy factors x and y via Equation (3).

$$r = \frac{\sum [(x_i - x_m) \times (y_i - y_m)]}{\sqrt{(x_i - x_j)^2} \times \sqrt{(x_i - x_j)^2}}. \quad (3)$$

Here, x_i and y_i denote the values of any two alloy factors associated with the i-th sample, whereas x_m and y_m correspond to the mean values of these two alloy factors in the property dataset. When $|r|$ exceeds 0.95, the alloy factors x and y are strongly linearly correlated, demonstrating that these parameters provide redundant information for material properties. To mitigate multicollinearity, the factor with lower importance ranking was systematically eliminated, and this iterative elimination process was not terminated until the top 10 most influential alloy factors were identified.

Step III: exhaustive calculation. The optimal combination for the highest property prediction accuracy was identified from the top 10 strongly correlated alloying parameters and thus defined as the key factor. During modeling, a random partition of the property dataset was performed into training and testing subsets at a ratio of 4:1. The training subset was adopted to develop an exhaustive calculation model, followed by the optimization of its parameters via a 10-fold cross-validation (CV) method. The model accuracy was evaluated via the mean absolute percentage error (MAPE)[32]. Then, the key alloy factors influencing UTS, YS, and EL were chosen according to the MAPE value of the exhaustive calculation model.

2.3. Machine learning

To maintain methodological rigor and prevent potential data contamination, the predictive models were systematically evaluated by stratifying 10-fold cross-validation (CV) with a completely independent test set. For this regression task with a limited sample size, six candidate algorithms were systematically evaluated, including XGBoost, Random forest regression (RFR), Gaussian process regression (GPR), decision tree (DT), k-nearest neighbors (KNN) and support vector regression (SVR). The optimal predictive algorithm was identified through rigorous CV analysis, with selection criterion based on minimization of the mean absolute error (MAE) in property correlation prediction.

To validate the accuracy enhancement achieved by integrating PFs, we implemented a 10-fold CV scheme to gauge the robustness of the ML models against overfitting. Subsequently, we constructed three distinct ML models by leveraging the selected algorithm to predict UTS, YS, and EL, respectively. To ensure statistical robustness, each mechanical property model was trained over 1 000 independent iterations, with each iteration utilizing a randomly sampled 80% subset of the available training data. This approach mitigates overfitting while ensuring reproducibility in predictive performance.

2.4. SHAP analysis

The game-theory-derived SHAP method was employed to elucidate the UTS, YS, and EL models, enabling quantitative analysis of the contributions from alloying elements and heat treatment parameters. By adopting additive feature attribution methods, the SHAP algorithm can approximate the output of the "black-box" model as a linear superposition of input feature functions and interpret each sample via Equation (4)[25].

$$f(x) = \phi_0 + \sum_{i=1}^{M} \phi_{ij}(x) \ . \quad (4)$$

Here, $f(x)$ is the predicted tensile property value, and ϕ_0 refers to the base value, which is typically obtained as the mean predicted value over the training set, indicating the expected output of the model in the absence of any input feature information. M indicates the number of input features, and $\phi_{ij}(x)$ represents the feature attribution value, indicating the contribution of the i-th input feature to the property for the j-th sample.

In this work, SHAP analysis was strategically implemented to bridge data-driven interpretation with alloy design, focusing on the following two key aspects: (i) quantitative ranking of alloying elements. A definitive compositional hierarchy can be established via the weight calculation method proposed by Jiang et al.[19], providing a data-driven foundation for achieving an optimal strength−ductility balance. (ii) identification of the dominant heat treatment parameters. The global sensitivity analysis capability of SHAP can be leveraged to evaluate the relative importance of all the heat treatment parameters based on the mean |SHAP value|. Consequently, the most influential candidate alloying elements and heat treatment parameters can be identified via the SHAP-guided analysis for multi-objective optimization design.

2.5. Multi-objective optimization design

Based on the python multiobjective optimization (Pymoo) framework, the multi-objective optimization design framework was developed by integrating the established UTS, YS, and EL predictive models with the non-dominated sorting genetic algorithm (NSGA-III)[33]. The search ranges for the element content and heat treatment parameters were established by combining candidate elements and the required heat treatment. The evolutionary computation parameters were configured with an initial population size of 1 000, maximum number of generations of 5 000, a crossover probability of 0.7, and a mutation probability of 0.2. Therefore, the Pareto front was successfully constructed, enabling the determination of the optimal element content and heat treatment parameter combinations for synergistically optimized mechanical properties.

2.6. Experimental validation

The fabrication of UHSDS specimens was performed utilizing a FL-1500 1.5 kW fiber laser equipped with a water-cooling and coaxial powder-feeding system. The laser processing parameters are as follows[34]: laser beam size, 1.2 mm; laser power, 430 W; laser scanning speed, 480 mm·s^{-1}; overlap ratio, 50%; and powder feeding rate, 6.5 g·min^{-1}. Nitrogen (N_2) of 99.999% purity was delivered as the shielding and carrier gas at 10 L·min^{-1}, by which the following three main effects could be produced via in-situ nitriding[35]: (i) interstitial solid solution. The N addition can facilitate the formation of a solid solution of interstitial C and N atoms in UHSDS; (ii) nano-precipitation. The precipitation of nano-sized nitrides can significantly enhance the mechanical properties and (iii) grain refinement. The prior austenite grain and the resulting martensite lath can be refined due to the reduction of the Ms temperature and the peritectic reaction rate, improving both the strength and ductility simultaneously. The as-deposited specimen (60 mm × 30 mm × 4 mm) was subsequently treated via a single-step tempering under the recommended parameters derived from ML.

Flat UHSDS specimens were obtained after ∼1 mm from the top surface by grinding. The loading axes of all the tensile specimens were set parallel to the laser scanning direction during machining. A constant crosshead speed of 0.2 mm·min^{-1} was applied during tensile testing on a universal testing machine (PWSE100). For each condition, the tensile properties were determined by calculating the average of three separate measurements. To ensure repeatability and reliability, three tensile specimens were tested for each condition. Furthermore, an electrochemical workstation (CS300) was employed to test corrosion resistance in a 3.5 wt% NaCl solution at room temperature. The potentiodynamic polarization curves were recorded at a scanning rate of 0.5 mV·s^{-1} over the potential range from −1.0 V to +0.5 V in a standard three-electrode cell. The UHSDS specimen, saturated calomel electrode, and platinum electrode were functioned as the working electrode, reference electrode, and counter electrode, respectively. The potentiodynamic polarization curves were fitted via Zview software, and the results for each condition are the average value calculated from three independent test samples.

A spark optical emission spectrometer (spark-OES, M4000 CCD) was used to determine the chemical composition of the UHSDS specimens. Phase identification was executed via X-ray diffraction (XRD, SmartLab) by employing a Cr source. An accelerating voltage of 40 kV and a current of 40 mA were applied, with a scanning 2θ range of 20°–90° at a constant angular step of 2°·min^{-1}. The microstructure examination of the specimens was carried out on a scanning electron microscope (SEM, MERLIN) operating at an accelerating voltage of 20 kV. Electron backscattered diffraction (EBSD) maps were acquired on an FEI Nova NanoSEM 450 at 20 kV with a step size of 0.15 μm and processed using Azteccrystal software. A transmission electron microscope (TEM, JEOL-2100) operated at 200 kV was employed for examining the detailed microstructural features. The TEM specimens were punched from mechanically ground thin foils and subsequently electropolished at 25 °C in a solution of 10% perchloric acid and 90% ethanol.

3. Results

3.1. Distribution characteristics of the property datasets

Figure 2 presents the data distribution in property datasets. As seen from Figure 2(a), the statistical distribution of the elemental compositions in steels exhibits the number of alloying elements spanning exclusively from 5 to 11. The compositional diversity and complex elemental interactions in these multi-component steels could expand the sample information space, thereby enhancing the generalizability of the ML models. Meanwhile, such complexity can pose obvious challenges in achieving the optimal steel composition and balanced property enhancement.

Figure 2(b) illustrates the distribution map of the elemental compositions within the mechanical property dataset. Apparently, Ni has the widest concentration range (0–19 wt%), followed by Cr and Co, with maximum concentrations exceeding 15 wt%. Cu and Mo show upper limits surpassing 5 wt%, whereas Al displays a more restricted solubility range of 0–3.4 wt%. The remaining trace elements are primarily distributed within the 0–1 wt% range. To increase the computational efficiency in ML applications, the search boundary for each alloying element was constrained according to the elemental distribution profiles, thereby mitigating the computational burden associated with high-dimensional composition space exploration.

Figure 2(c) shows the distribution of heat treatment (HT) types and parameters within the dataset. Clearly, there are three HT categories, including multi-step HT (solid solution treatment + tempering), single-step HT (tempering), and without HT. The temperature of the solid solution (SS) treatment varies from 427 °C to 1 150 °C, with a holding time range of 0.5–4 h. The tempering temperature changes from 200 °C to 620 °C, with a holding time range of 0.08–12 h.

Figures 2(d)–(f) depict the distributional characteristics of the mechanical properties within the dataset, with UTS values

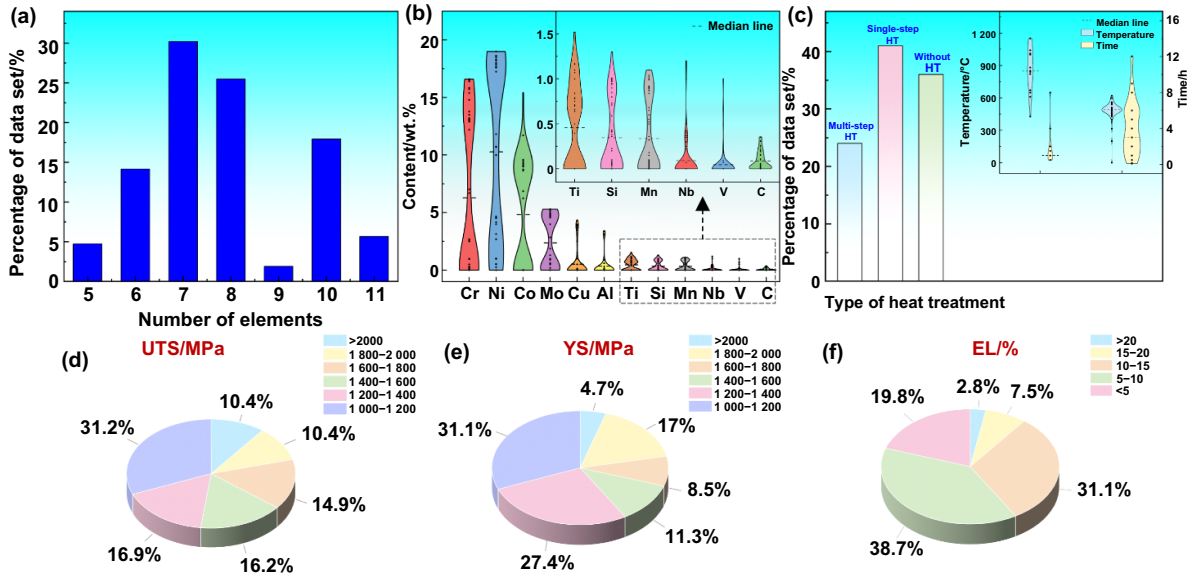

Figure 2. Data distribution in property datasets. (a) Distribution map of steel composition. (b) Distribution map of element and their contents. (c) Distribution map of heat treatment parameters, Pie chart distribution of properties range, (d) UTS, (e) YS, and (f) EL.

ranging from 1 218 MPa to 2 217 MPa, YS values ranging from 1 005 MPa to 2 092 MPa, and EL values ranging from 1.2% to 25.5%. Notably, 69.8% of specimens exhibit UTS and YS values within the range of 1 200–1 800 MPa and 1 000–1 600 MPa, respectively. Furthermore, 41.5% of the samples achieved EL values exceeding 10%.

3.2. Key alloy factor screening

Figure 3 presents the screening procedure and key alloy factors. After the importance ranking, the top 15 alloy factors were identified, as shown in Figures 3(a)–(f). Among them, a strong correlation exists between A8-1 and S21-1 for UTS, along with a similarly strong linear interdependence among A5-1, C3-1, and S22-1. In the case of the YS, there is a strong correlation between C16-2 and A8-1, whereas S22-1, C16-2, E11-1, E14-1 and A5-1 constitute another interconnected group. Regarding EL, the data indicates a linear dependence between C16-2 and A8-1, while E9-1, A8-1 and C11-1 exhibit a separate strong correlation. Based on the aforementioned criteria, the lower-ranking alloy factors within the strongly correlated groups were eliminated, and the remaining 10 alloy factors selected for exhaustive analysis are listed in Table 2.

Figures 3(g)–(i) show the results of the exhaustive screening process, indicating that the error level can be minimized by combining 2-5 alloy factors. Clearly, the reduced variable dimension and improved design efficiency can be achieved via the exhaustive method. When the number of alloying factors is three, the error for the UTS model is minimized at 7.6% for the combination of S17-2, C12-1, and C14-1. Conversely, the smallest error of 9.9% for the YS model is achieved by considering two alloy factors, with the combination of E11-1 and S17-2. Additionally, the EL model shows the lowest error of 20.9%, with two alloy factors corresponding to E9-1 and C9-1. In this work, we define {S17-2, C12-1, C14-1}, {E11-1, S17-2}, and {E9-1, C9-1} as the key alloy factors influencing the UTS, YS, and EL, respectively. These key alloying factors are related to the atomic and electronic size, lattice constant and electrochemical characteristics of the material (see Table 3).

3.3. Machine learning algorithm selection and model establishment

Figures 4(a)–(c) present the preliminary results of algorithm screening. The XGBoost algorithm clearly has the lowest MAE during 10-fold cross-validation for the three mechanical properties, with values of (125 ± 22.9) MPa for the UTS, (138.0 ± 34.2) MPa for the YS and (2.5 ± 0.4)% for the EL. The dispersion of the prediction errors was assessed via the coefficient of variation (CV = standard deviation/mean × 100%), a metric adopted to normalize the data spread for comparative analysis[36]. The calculated CVs for the MAEs of the UTS, YS and EL are 18.32%, 24.78% and 16.00%, respectively. This moderate level of variability is acceptable, given that the model is in preliminary status without hyperparameter optimization[37]. These results indicate that the XGBoost algorithm exhibited the highest predictive accuracy among the evaluated models and was therefore chosen for subsequent analyses. The prediction errors are illustrated in Figures 4(d)–(f), with an R^2 of 0.914, an MAE of 57.344 MPa and an RMSE of 77.861 MPa for the training set of the UTS model, an R^2 of 0.939, an MAE of 40.467 MPa and an RMSE of 61.216 MPa for the training set of the YS model, an R^2 of 0.886, an MAE of 1.071% and an RMSE of 1.602% for the training set of the EL model. Comparatively, the values of R^2, MAE and RMSE for the training set are close to those for the test set, with R^2 differences of less than 0.05. Therefore, the constructed models for UTS, YS, and EL demonstrate good predictive accuracy and generalization capability[38].

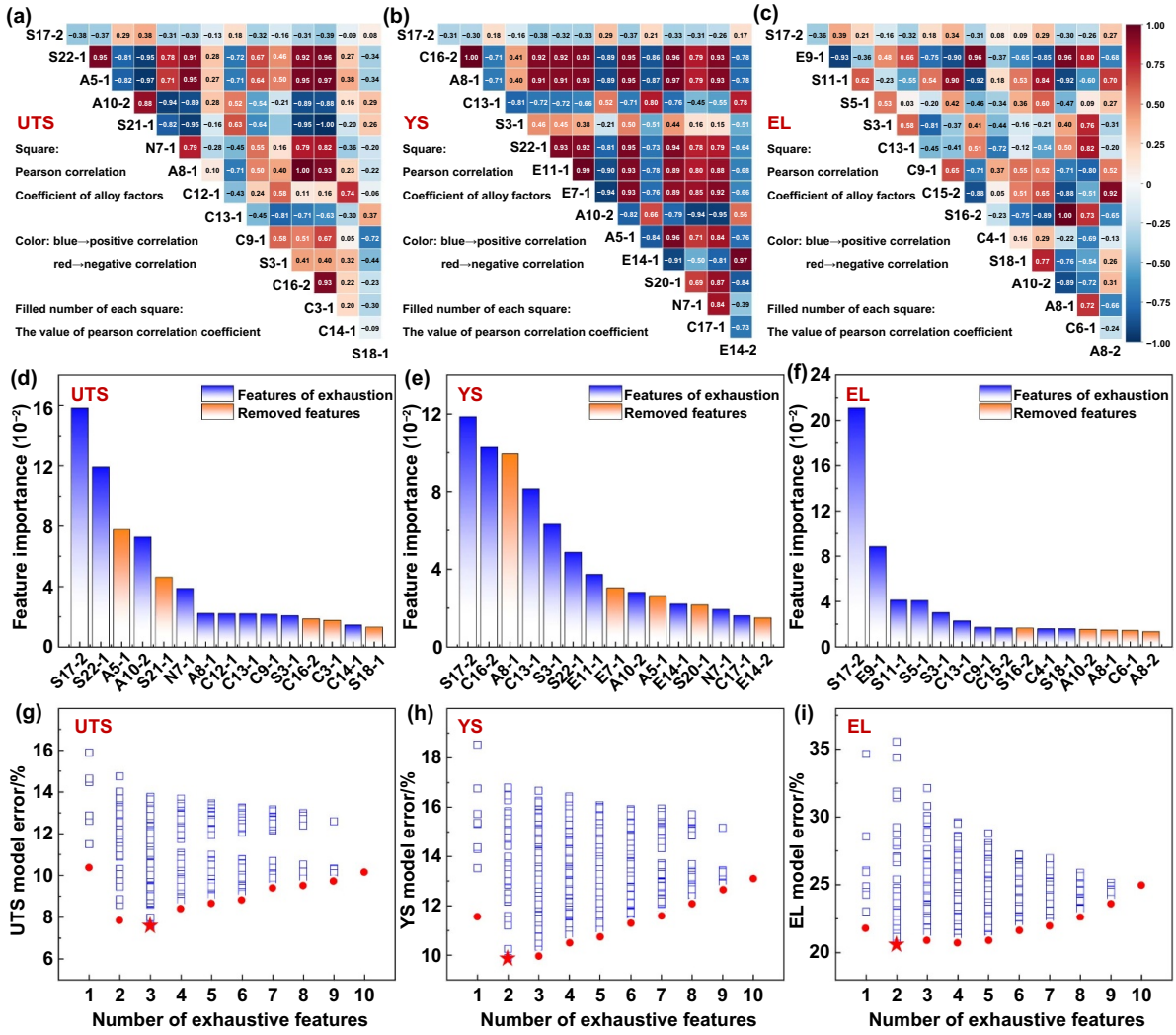

Figure 3. Screening process and results of key alloy factors. (a)–(c) Pearson correlation of the top 15 alloy factors in importance ranking, (d)–(f) The top 15 alloy factors in importance ranking, and the alloy factors shown in blue are those that are excluded in the correlation. screening; (g)–(i) Exhaustive calculation results of alloy factors.

Table 2. The top 10 alloy factors for exhaustive calculation.

Properties	UTS	YS	EL
No strong linear correlation, ranking the top 10 alloy factors	S17-2, S22-1, A10-2, N7-1, A8-1, C12-1, C13-1, C9-1, S3-1, C14-1	S17-2, C16-2, C13-1, S3-1, S22-1, E11-1, A10-2, E14-1, N7-1, C17-1	S17-2, E9-1, S11-1, S5-1, S3-1, C13-1, C9-1, C15-2, C4-1, S18-1

3.4. Selecting elements and postheat treatment based on SHAP analysis

SHAP analysis was applied to elucidate the underlying mechanisms of the three PF-ML models for UTS, YS and EL, with the results shown in Figures 5(a)–(c). Each numerical point represents an individual sample, with its color indicating the key alloy factor value. A positive SHAP value indicates that this key alloy factor contributes positively to the property, whereas a negative value denotes an adverse effect. A SHAP value close to zero suggests that the corresponding key alloy factor has a negligible influence on the property.

Based on the weight calculation method proposed by Jiang et al.[19], the coefficient K_{ni} (key alloy factor influence coefficient) was estimated from the slope of the best-fit line between the key alloy factor values and their corresponding SHAP values. The element ranking weight coefficients Z_{ni}, associated with each key alloy factor are summarized in Table 4.

The sign of K_{ni} dictates the orientation (positive/negative) of the monotonic correlation between the critical steel characteristic and the target property, while the absolute magnitude of K_{ni} quantifies the intensity of such a correlation's influence[19]. Figures 5(a)–(c) illustrate the explicit associations between key alloy factors and the corresponding properties. By considering these associations alongside the influence coefficients in Table 4, the significance of elements on properties can be analyzed systematically. There are 13 elements available for designing UHSDS, including C, Cr, Ni, Si, Mn, Co, Mo, Al, Nb, V, Cu, and Ti. Figures 5(d)–(j) rank

Table 3. The key alloy factors obtained by recursive elimination.

Properties	Key alloy factors	Description
UTS	S17-2	The square of the deviation from sound propagation rate in the element compared with iron C^2
	C12-1	The thermal conductivity k
	C14-1	The diffusion activation energy of elements in iron E_i
YS	E11-1	The number of effective nuclear charge Z_e
	S17-2	The square of the deviation from sound propagation rate in the element compared with iron C^2
EL	E9-1	The number of work function ϕ
	C9-1	The compression modulus M_c

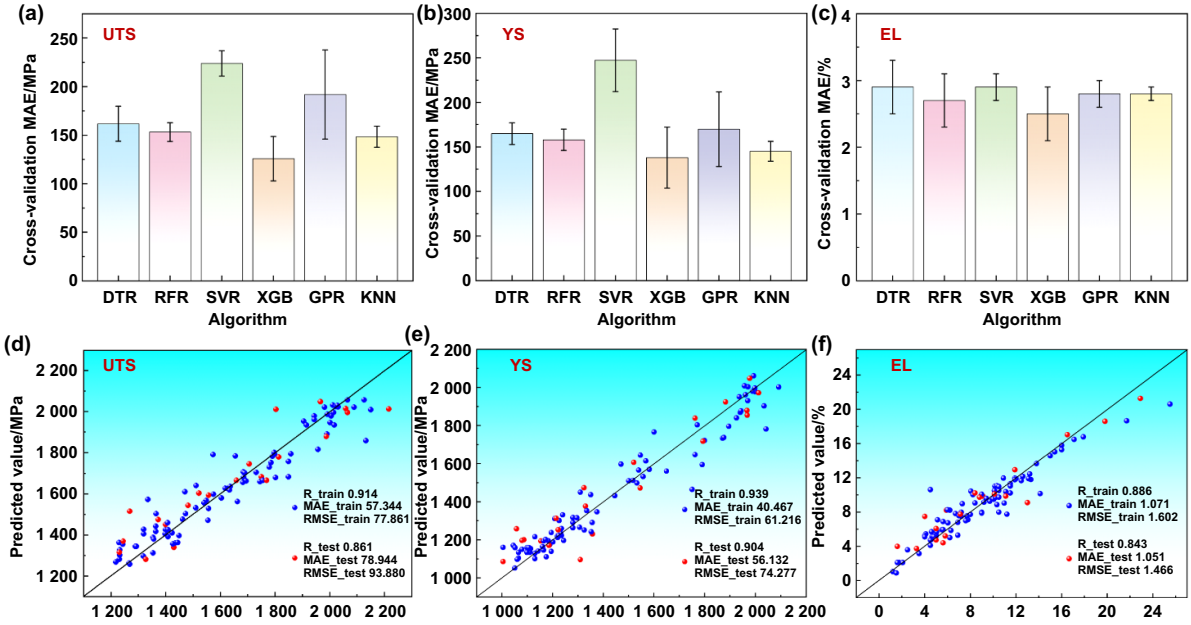

Figure 4. Algorithm screening and ML model predictions. (a)–(c) The mean cross-validation results of different ML algorithms, (d)–(f) the model predictions with the key alloy factors as inputs.

Table 4. Key alloy factors, key feature quantity influence coefficient K_{ni}, and element ranking weight coefficient Z_{ni}.

Properties	UTS			YS		EL	
Key alloy factors	S17-2	C12-1	C14-1	E11-1	S17-2	E9-1	C9-1
K_{ni}	−198.08	−56.02	−48.13	190.19	−182.52	2.13	−9.74
Z_{ni}	0.218	0.062	0.053	0.245	0.255	0.096	0.404

the importance of the above 13 elements on the three target properties based on key alloy factors, respectively.

Table 4 provides the elemental importance ranking corresponding to the seven key factor quantities via the calculation of the weight coefficients. Accordingly, the comprehensive elemental importance ranking affecting the overall alloy properties is presented in Figure 5(k). A lower comprehensive element ranking value corresponds to a greater influence on comprehensive properties. As shown in Figure 5(k), the influence of alloying elements on the enhancement of the overall properties follows a descending order. Considering the high cost of Ti and Nb, we selected Si,Cu and Al as the candidate alloying elements to enhance the comprehensive properties of UHSDS. In addition, Mn is typically contained in carbon steels, and Cr with a content above 12 wt% was designed to ensure the corrosion resistance. Furthermore, Ni was introduced as an additional candidate element to balance the phase fractions.

Figure 5(l) shows the comprehensive normalized Mean |SHAP value| of heat treatment, revealing that the tempering temperature and holding time are the predominant factors governing the overall mechanical properties. Consequently, a single-step tempering was selected as the post heat treatment, and its parameter ranges are detailed in Table 5.

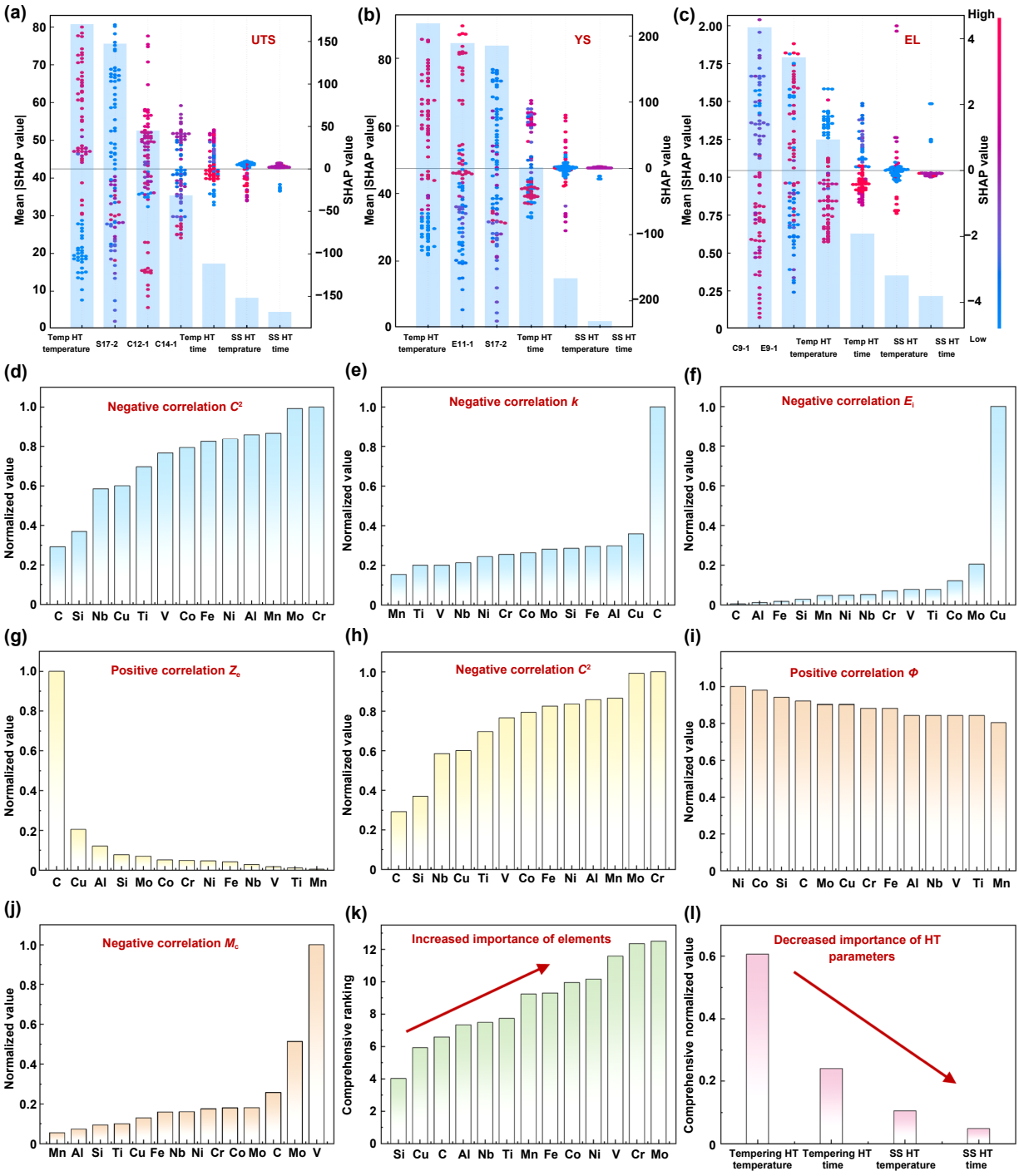

Figure 5. SHAP analysis. SHAP values of inputs affecting properties. (a) UTS, (b) YS, and (c) EL, ranking the importance of elements. affecting properties based on different alloy factors, (d) S17-2, (e) C12-1, (f) C14-1, (g) E11-1, (h) S17-2, (i) E9-1, (j) C9-1, (k) comprehensive rank of element after weighted calculation, (l) comprehensive normalized Mean |SHAP value| of heat treatment.

Table 5. Search scheme for the alloy composition (wt%) and heat treatment parameters.

Search space	Si	Cu	C	Al	Mn	Ni	Cr	Tempering temperature/°C	Tempering time/h
Lower limit	0	0	0	0	0	0	12	400	0
Upper limit	1	1	0.3	1	1	4	16	600	12

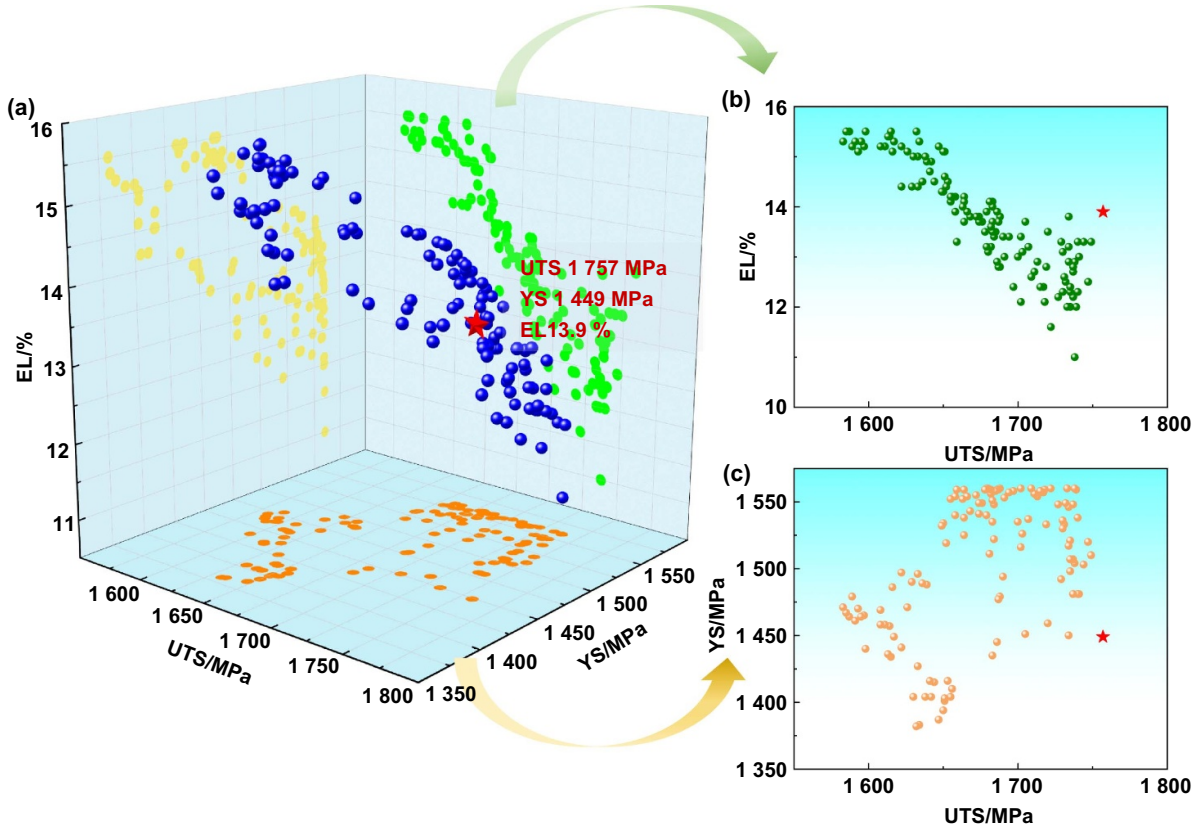

Figure 6. Multi-objective optimization results via machine learning. (a) Three-dimensional Pareto front of UTS, YS, and EL, (b) two-dimensional Pareto front of UTS and EL, (c) two-dimensional Pareto front of UTS and YS.

3.5. Novel ultra-high strength and ductile steel

Leveraging the Pymoo framework, the predictive models for UTS, YS and EL were embedded prior to implementing a multi-objective optimization system via NSGA-III integration. With SHAP analysis, the optimization ranges for the chemical composition and heat treatment parameters were determined as input variables (Table 5). Subsequently, The Pareto front characterizing the strength and ductility trade-offs was generated via the NSGA-III. Within this optimized solution space, the recommended compositions and processing parameters are demarcated by blue dots in the three-dimensional Pareto front (Figure 6(a)). In general, the spatial distribution of these points map out a well-defined performance boundary surface[39]. Figure 6(b) illustrates the UTS-YS projection by green dots, revealing a significant synergistic relationship between the UTS and YS. In contrast, the UTS-EL relationship is mapped via orange dots in Figure 6(c), demonstrating the characteristic strength−ductility trade-off. A confined "knee" region is recommended, where a minimal sacrifice in strength is offset by a considerable improvement in ductility[40]. To reconcile high EL with the requisite strength, an optimal solution corresponding to a novel UHSDS sample exhibiting model-predicted properties of UTS 1 757 MPa, YS 1 449 MPa and EL 13.9% was selected for experimental validation.

Herein, a 480 °C × 6 h single-step post-heat treatment was predicted, which is consistent with our design concept (Figure 1). In fact, the ML models were employed to predict the mechanical properties after a multi-step tempering heat treatment (not shown here), demonstrating that the much more complex tempering processes cannot provide a decisive improvement in tensile properties compared with single-step tempering. Additionally, the experimental work of Tan et al.[41] demonstrated that a 490 °C × 4 h single-step tempering process achieved a balanced property profile (UTS: 1 656 MPa, YS: 941 MPa and EL: 18.3%), which was slightly inferior to that (UTS: 1 732 MPa, YS: 1 153 MPa and EL: 16.5%) after a 472 °C × 2 h + 490 °C × 4 h multi-step tempering process for the AISI 420 alloy. Given the inherent advantages of process simplicity, reproducibility and industrial viability, single-step tempering was conclusively justified as the superior choice for the designed composition. Accordingly, the predicted and experimentally measured compositions, along with the corresponding mechanical properties, are tabulated in Table 6.

The tensile curves of the UHSDS specimens are presented in Figure 7(a). The as-deposited specimen exhibits a UTS of (1 370 ± 21) MPa, a YS of (934 ± 26) MPa and an EL of (8.7 ± 0.5)%. In contrast, a simultaneous enhancement in both strength and ductility was achieved after a 480 °C × 6 h single-step tempering heat treatment, with a UTS of (1 713 ± 17) MPa, a YS of (1 502 ± 33) MPa and an EL of (15.5 ± 0.7)%. This corresponds to an approximately 30% increase in UTS, accompanied by a twofold improvement in ductility. Notably,

Table 6. Predicted vs measured chemical composition (wt%) and tensile properties of the developed UHSDS.

Steel	Si	Cu	C	Al	Mn	Ni	Cr	UTS/MPa	YS/MPa	EL/%
UHSDS-Pre.	0.56	0.60	0.16	0.40	0.76	3.20	15.01	1 757	1 449	13.9
UHSDS-Exp.	0.58	0.62	0.15	0.37	0.82	3.15	15.16	1 713 ± 17	1 502 ± 33	15.5 ± 0.7

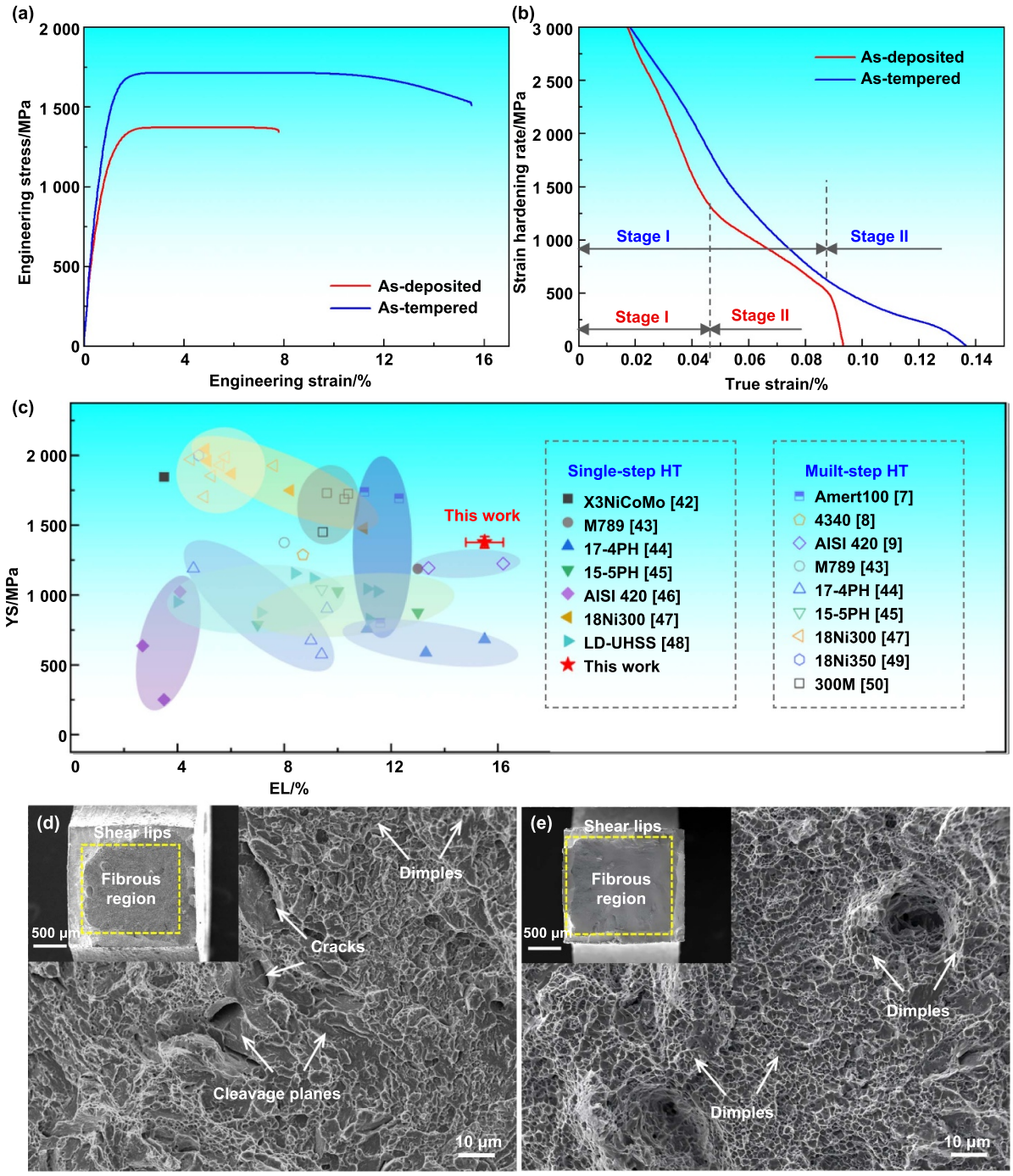

Figure 7. Mechanical properties and fractography of the as-deposited and as-tempered UHSDS specimens. (a) Engineering stress−strain curves, (b) strain work-hardening rate curves, (c) comparison of tensile properties among the reported laser additively manufactured steels after a single-step HT and a multi-step HT, (d) fracture morphology of as-deposited specimen, (e) fracture morphology of as-tempered specimen.

all measured tensile properties exhibit exceptionally low CVs of <5%, indicating the high consistency and reliability of the experimental process.

To understand the deformation behavior, the strain hardening rates of the UHSDS specimens were calculated, as presented in Figure 7(b). Apparently, the strain hardening rate of the as-tempered sample is greater than that of its as-deposited counterpart throughout both stage I (elastic deformation) and stage II (plastic deformation). This superior hardening behavior of the as-tempered UHSDS, in good agreement with the twofold enhancement of ductility, could be correlated with the profuse formation of precipitates, which will be further discussed hereinafter.

Figure 7(c) compares the tensile properties of the as-tempered UHSDS designed in this work with those of previously reported additively manufactured steels after a single-step[42–48] or a multi-step[7–9,43–45,47,49,50] postheat treatment. The as-tempered UHSDS exhibits superior tensile properties over all the single-step heat treated steels, and demonstrates higher elongation at the equivalent strength level relative to multi-step heat treated counterparts. In addition, Supplementary Material 3 provides a comparison of the chemical composition, post-heat treatment and mechanical property of the newly developed UHSDS and additively manufactured commercial ultrahigh-strength steels. Apparently, this work achieves an excellent strength−ductility balance, exhibiting overwhelming superiority in cost effectiveness and process simplicity over other steels.

Figures 7(d) and (e) present the fracture surfaces of the UHSDS specimens, showing apparent necking deformation with respect to the fiber area and shear lip. The fracture surface morphology of the as-deposited specimen features large cleavage planes, cracks, and tearing ridges, demonstrating a typical mixed-mode fracture (Figure 7(d)). Comparatively, the as-tempered specimen is characterized by ductile fracture with massive dimples and a larger fiber area, demonstrating an overall increasing trend in ductility, as shown in Figure 7(e). The dimple size and density of the specimens were quantified by ImageJ software, yielding values of 0.79 μm and 7×10^9 dimples·μm^{-2} for the former and 1.02 μm and 6.3×10^{10} dimples·μm^{-2} for the latter. It is widely accepted that the dimple areal density on a fracture surface is governed by the population of nucleation sites and the ductility of the material[51,52]. Therefore, the ductility was evidently enhanced after a single-step tempering HT for the LDED UHSDS, which is in good agreement with the ductility enhancement, as demonstrated in Figure 7(a).

3.6. Microstructure analysis

Figure 8 presents the phase constituents, microstructural morphology, and dislocation characteristics of the LDED-fabricated UHSDS specimens. As seen from the XRD spectra (Figure 8(a)), the as-deposited specimen is predominantly composed of martensite (M), austenite (A), $M_{23}C_6$ carbide, and AlN phase. In comparison, stronger M peaks together with the occurrence of NiAl and ε-Cu are detected in the as-tempered specimen. SEM micrographs (Figures 8(b) and (c)) confirm the presence of high-density precipitates within the martensite laths of the UHSDS specimen after the single-step tempering treatment.

To further elucidate the spatial distributions of crystallographic orientations, interphase boundary characteristics, and dislocation-induced lattice distortions, the EBSD analysis was performed, as shown in Figures 8(d)–(i). Inverse pole figure (IPF) maps and pole figures (PFs) are presented in Figures 8(d) and (g), respectively. The as-deposited specimen exhibits a local <001> texture, as evidenced by a maximum multiple of uniform density (MUD) of 5.29 (Figure 8(d)). Interestingly, this texture slightly intensified after the tempering treatment, with the MUD value increased to 5.61 for the as-tempered specimen (Figure 8(g)). Although the texture is generally weakened by dislocation recovery and recrystallization during tempering, the observed increase in <001> texture intensity indicates the preferential growth of grains with <001> orientation. This anomalous phenomenon may be attributed to the pinning effects of the precipitated phases. As indicated by the phase distribution map (Figure 8(e)), the as-deposited sample is composed of 75.7% α-Fe (red) and 24.3% γ-Fe (blue). After the tempering treatment, the α-Fe content increased to 82.3%, whereas the γ-Fe is reduced to 17.7%, which is consistent with the change in the XRD peak intensities of M and A (Figure 8(a)). Figures 8(f) and (i) compare the geometrically necessary dislocation (GND) distributions, indicating a GND density of 1.93×10^{15} m^{-2} and 1.86×10^{15} m^{-2} for the as-deposited and the as-tempered specimens, respectively. This phenomenon is closely associated with the dislocation annihilation after tempering heat treatment[53].

To elucidate the detailed microstructural characteristics, TEM characterization of the LDED-fabricated UHSDS specimens with different states was carried out, as shown in Figure 9. The as-deposited specimen consists predominantly of a lath-shaped M matrix, with sparsely distributed A as well as nano-precipitates $M_{23}C_6$ and AlN identified by selected-area electron diffraction (SAED) analysis (Figures 9(a)–(d)). In comparison, M and A retained with slightly coarsened size, whereas a much larger volume fraction of nano-sized particles can be observed in the as-tempered specimen (Figures 9(e)–(g)). Specifically, the NiAl and ε-Cu phases, which precipitated during the tempering treatment, have been detected in Figure 9(h). The remarkably high coherence between NiAl and α-Fe, as demonstrated in previous studies regardless of heat treatment conditions[54–56], was further verified by SAED pattern analysis.

3.7. Corrosion resistance

Figure 10 presents the potentiodynamic polarization results and electrochemical impedance spectra of the specimens in a 3.5 wt% NaCl solution. Comparative analysis reveals a clear performance hierarchy: the as-tempered specimen > AISI 420 steel specimen > as-deposited specimen. The polarization curves and fitting results revealed that the as-tempered specimen exhibited a 0.167 V increase in corrosion potential (E_{corr}), a 2.5×10^{-5} A·cm^{-2} reduction in corrosion current density (J_{corr}) and an over order of magnitude in corrosion

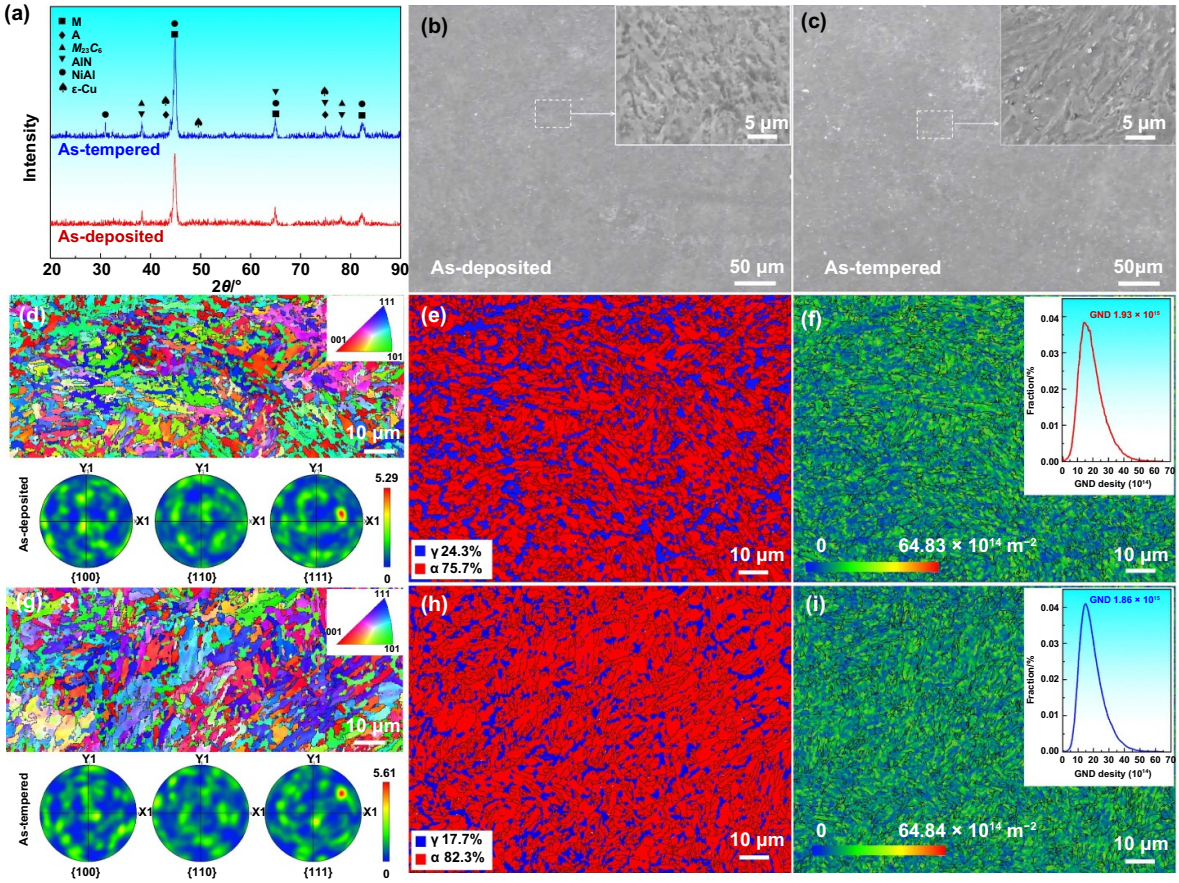

Figure 8. XRD, SEM and EBSD characterizations of the specimens. (a)XRD spectra, (b) and (c) SEM micrographs, (d), (g) inverse pole figure map and pole figure map, (e), (h) phase map, (f), (i) GND map with inset of GND density distribution curve.

rate decrease (Figures 10(a) and (b)). The high reproducibility of these electrochemical measurements is quantified via CV, with key parameters such as J_{corr} for the as-tempered specimen showing an extremely low CV value of only 2.01%. This remarkably low data dispersion across triplicate tests attests to the high consistency and reliability of our experiment. In general, the elevated E_{corr} value can be interpreted as an enhanced passivation capability, which effectively suppresses the initiation of localized corrosion reactions[57]. Meanwhile, the reduced J_{corr} confirms the inhibitory effect of the tempering treatment on the charge-transfer kinetics, thereby retarding the overall corrosion process[58].The impedance spectra were fitted and analyzed using ZView software, as shown in Figures 10(c) and (d). Both specimens are characterized by a single capacitive arc, indicating similar electrochemical behavior. Compared with the as-deposited specimen and AISI 420 steel, the as-tempered specimen has a markedly larger capacitive arc radius, demonstrating greater charge-transfer resistance and thus superior corrosion resistance[59].

As illustrated in Figure 10(d), the impedance modulus in the mid-frequency range (10^2–10^4 Hz) exhibits a linear relationship with frequency, indicating capacitive behavior. Therefore, corrosion resistance was enhanced by the impediment of electron transfer and the accumulation of ions on the sample surface. Furthermore, the as-tempered sample has a significantly greater phase angle across the 10^0–10^2 Hz frequency range in contrast to the as-deposited sample. It has been reported that a larger phase angle is attributed to enhanced charge transfer resistance in NaCl solution, further confirming improved corrosion resistance[60].

Figure 10(e) presents the quantitative analysis results of the EIS data by employing an equivalent circuit model. The model consists of solution resistance (R_s), charge-transfer resistance (R_t), and a constant phase element (CPE_1). The R_s values of all three specimens were found to be comparable, which is consistent with the similar impedance modulus trends observed in the high-frequency region (10^4–10^5 Hz) (Figure 10(d)). The R_t value of the as-tempered specimen was measured as 17 253 Ω·cm^2, representing approximately 5-fold and 3-fold increment compared with those of the as-deposited specimen (3 704 Ω·cm^2) and AISI 420 steel (6 236 Ω·cm^2), respectively. Furthermore, a significantly higher CPE_1 value was observed for the as-tempered specimen relative to both the as-deposited specimen and the AISI 420 steel. These results collectively indicate that tempering promotes the formation of a passive film on the as-deposited specimen, which exhibits higher stability in 3.5 wt% NaCl solution and effectively suppresses electrochemical reactions between the corrosive medium and the specimen surface.

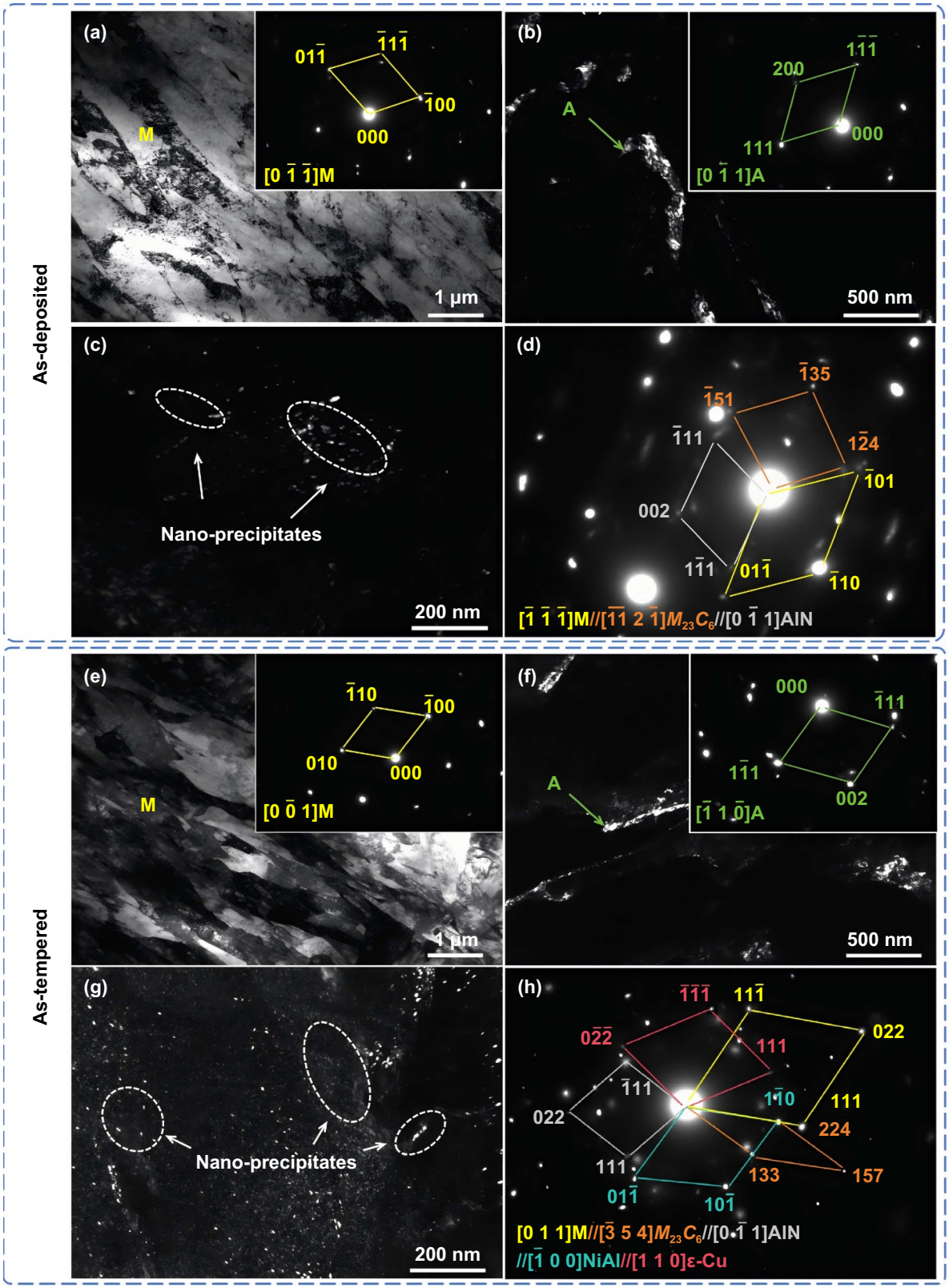

Figure 9. TEM results of the LDEDed as-deposited and as-tempered specimens. (a), (e) bright-field (BF) image and SAED pattern of M, (b), (f) dark-field (DF) image and SAED pattern of A, (c), (g) DF image of nanoprecipitates, (d), (h) SAED pattern of nanoprecipitates and M.

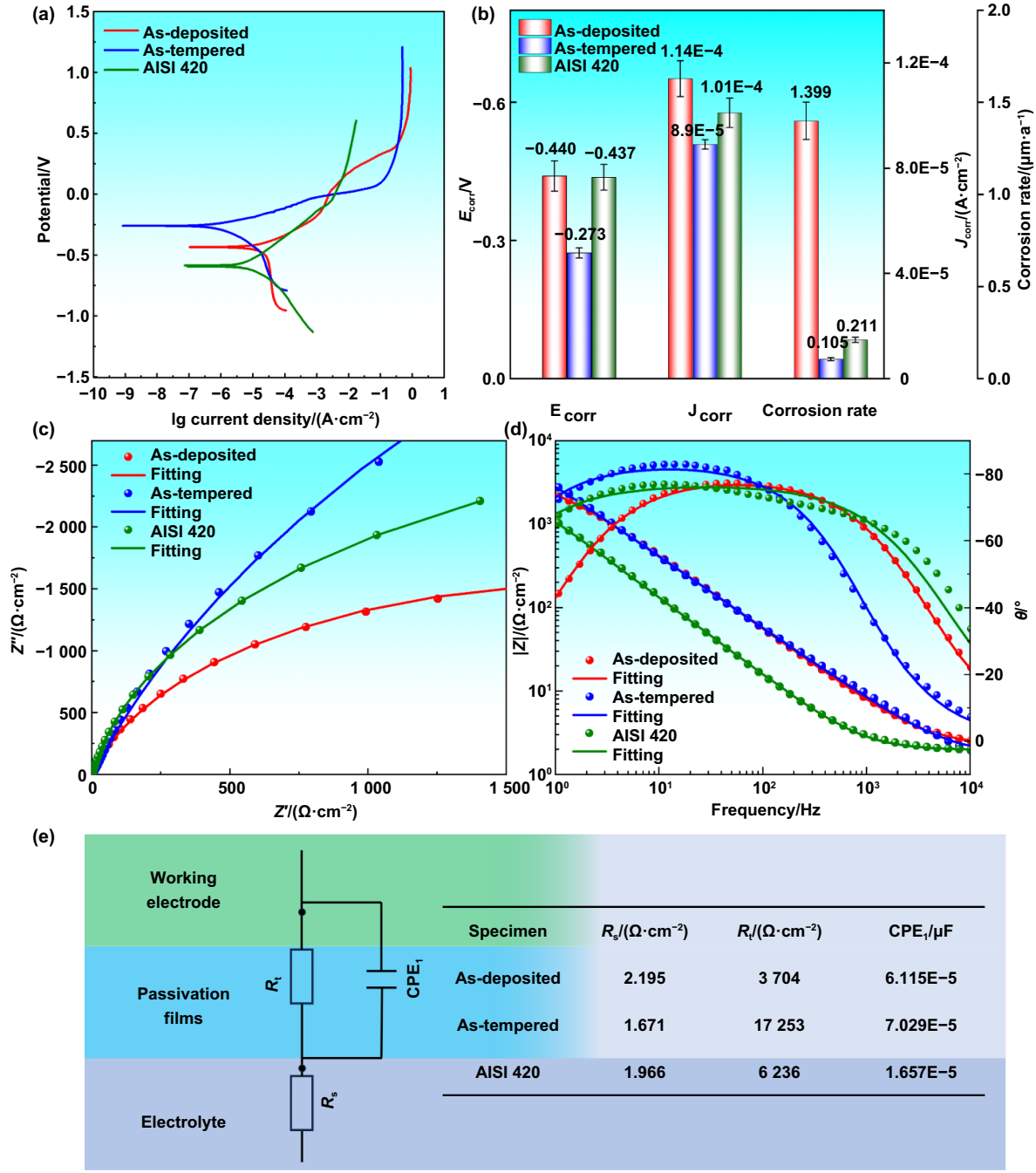

Specimen	R_s/(Ω·cm^{-2})	R_t/(Ω·cm^{-2})	CPE$_f$/μF
As-deposited	2.195	3 704	6.115E−5
As-tempered	1.671	17 253	7.029E−5
AISI 420	1.966	6 236	1.657E−5

Figure 10. Potentiodynamic polarization results and electrochemical impedance spectra of the specimens. (a) Polarization curves, (b)fitting results, (c) Nyquist scatter plots and fitted curves, (d) bode plots, (e) equivalent circuit diagram and schematic diagram.

4. Discussion

4.1. Model accuracy and methodology generalizability

In general, an ideal ML model can demonstrate high performance and maintain consistent behavior across training and testing datasets[10]. Such consistency under elevated accuracy can signify effective mitigation of overfitting, ensuring robust generalization to unseen datasets and model reliability. As shown in Table 7, for the UTS model, the predicted value is 1 757 MPa versus the experimentally determined average value of 1 713 MPa, with a deviation of 2.63%. For the YS model, 1 449 MPa is predicted compared to the experimental measurement of 1 502 MPa, yielding a deviation of 3.66%. For the EL model, the predicted and experimental values are 13.9% and 15.5%, respectively, with a deviation of 10.32%. Both the UTS and YS models exhibit deviations below 5%, while the absolute difference between the experimental and predicted values for EL is constrained within 3.5%, suggesting the high predictive accuracy of these three models.

Table 7. Comparison of predicted and experimental mean values with R^2_{Train}, R^2_{Test} and "over-fitting" index (R^2_{Test}/R^2_{Train}) of UTS, YS and EL model.

Performance metrics	UTS	YS	EL
Pre. value	1 757 MPa	1 449 MPa	13.9%
Exp. mean value	1 712 MPa	1 502 MPa	15.5%
Bias/%	2.63	3.66	10.32
R^2_{Train}	0.914	0.939	0.886
R^2_{Test}	0.861	0.904	0.843
R^2_{Test}/R^2_{Train}	0.942	0.963	0.951

To minimize overfitting for the ML models, we implemented a multi-pronged strategy including the aforementioned feature screening, algorithm selection, and independent iteration. According to the overfitting index (R^2_{Test}/R^2_{Train}), the values for the UTS, YS, and EL models are 0.942, 0.963, and 0.951, respectively. These near-unity values close to 1.0 confirm comparable predictive accuracies across the training and testing datasets, demonstrating the outstanding generalization capability[37]. Hence, the developed models are sufficiently robust and accurate for designing alloys excluded from the training set.

Noteworthily, the PF-ML approach has been applied in designing high-performance copper alloys[18], aluminum alloys[19] and high-entropy alloys[20], exhibiting potential generalizability in diverse alloy systems. Howbeit, there are two main limitations for the PF-ML approach. (i) Data restriction. The datasets obtained from extremely different fabrication processes are inherently incompatible due to the apparent discrepancy in the corresponding microstructural evolution behavior. (ii) Feature identification. The re-screening of key features must be carried out for each alloy system and its target outputs.

4.2. Essential intrinsic attributes of key alloy factors

Based on the aforementioned results, there are 6 key alloying factors affecting the UTS, YS, and EL. Among them, the key alloy factors S17-2, C14-1, and C12-1 are all negatively associated with the UTS. For S17-2, the variance in the acoustic-wave propagation velocity among different elements is quantified. In solid materials, the characteristics of sound transmission are fundamentally determined by the interatomic bonding configurations[61]. At the atomic scale, the longitudinal acoustic wave velocity ν_l is directly governed by the elastic constants of the lattice, following the relationship of $\nu_l = \sqrt{\frac{C_{11}}{\rho}}$, where ρ is the density and the constant C_{11} is the second derivative of the interatomic potential energy curve with respect to atomic displacement, which physically represents the bond stiffness[62,63]. The higher the acoustic wave velocities are, the stronger the interatomic bonding forces. Consequently, the macroscopic strength is substantially elevated because of the dislocation glide hindrance under the bond strengthening mechanism.

For C14-1, the parameter quantifies the mean diffusion activation energy of alloying elements within iron (Fe), representing the energy barrier for atomic diffusion through the Fe lattice[61]. It is well known that atomic diffusion in alloys primarily occurs via vacancy mechanisms, with the activation energy including the formation energy and the migration energy of vacancies[64]. The migration energy is critically influenced by the atomic size mismatch between solute and solvent (Fe) atoms according to the Zener strain field theory[65]. A larger solute atom can introduce greater lattice distortion upon moving into a vacant lattice site, leading to a higher energy barrier. Supersaturated solid solutions can be retained at room temperature for elements with low diffusion activation energies, resulting in the matrix strengthening induced by lattice distortion. Furthermore, the reduced diffusion activation energy facilitates the rapid formation of high-density nanoscale precipitates, prompting a pronounced increase in the *Orowan* strengthening[66]. Therefore, the synergistic effect of solid–solution strengthening and *Orowan* strengthening contributes to a significant increase in tensile strength.

For C12-1, it represents the mean number of thermal conductivity, which is primarily determined by the lattice vibrations and the free electrons' movement[61]. For metallic systems, the electronic contribution to thermal conductivity dominates, described by the Wiedemann–Franz law[67]: $K_e = L_0 \sigma T$, where L_0 is the Lorenz number, σ is the electrical conductivity, and T is the temperature. According to Matthiessen's additivity rule for resistors[68], the defect resistivity (inverse of conductivity) includes contributions from solute atoms, grain boundaries, and precipitates, all of which can scatter conduction electrons and thus reduce both σ and K_e. The strength can be enhanced due to the formation of solid solutions and grain refinement, but the thermal conductivity is reduced because an increase in grain boundaries can intensify the interfacial scattering effect[69]. Given that an indirect negative correlation exists between strength and thermal conductivity, ultrahigh-strength steels strengthened via multi-phase precipitation usually exhibit low thermal conductivity.

The YS reflects the capacity of materials to resist plastic deformation. The key alloy factor E11-1 serves as a descriptor of the mean effective nuclear charge (Z_{eff}), quantifying the net attractive force between the atomic nuclei and valence electrons[61], and exhibiting a positive correlation with the YS. An elevated effective nuclear charge is correlated with intensified nuclear binding forces, resulting in reduced atomic radii and increased ionization energies. A higher ionization energy can suppress the electron delocalization, promote the strengthened bonding cohesion and stabilize the precipitated phases. Consequently, the enhanced effective nuclear charge density enables the efficient atomic packing combined with the intensified precipitation strengthening. Elements with high Z_{eff} (e.g., Mo, V, and Nb) have a strong chemical affinity for C, favoring the formation of stable, coherent, or semi-coherent carbides. These carbides possess high cohesive energy and low interfacial energy with the Fe matrix, resulting in exceptional resistance to coarsening by Ostwald ripening at elevated temperatures[70]. Therefore, the macroscopic yield strength is

improved via the effective dislocation pinning owing to the increase in the dislocation motion resistance. The key alloy factor S17-2 has a similar effect on the YS as that observed for the UTS, demonstrating consistent negative correlations with both strengths.

In terms of EL, the key alloy factor E9-1 exhibits a positive correlation with EL, whereas C9-1 shows a negative correlation with EL. The descriptor E9-1 denotes the average work function, defined as the minimum energy required for electron emission from a material surface[61]. This property is fundamentally determined by the bulk electron density distribution and the formation of a surface dipole. From a bonding perspective, a high work function often correlates with stronger metallic bonding because of the higher energy required to remove an electron from the Fermi level[71]. The enhancement of the work function can be achieved by incorporating high-work function elements, resulting in increased free electron density and strengthened interatomic bonding[72]. Meanwhile, the multiple slip systems can be activated by the introduction of nanoscale precipitates, which promote the dislocation multiplication and delay the necking effectively, thereby enhancing the uniform elongation. The latter C9-1 represents the compression modulus, quantifying the ability for resisting the compressive deformation of a material. This parameter is fundamentally determined by the atomic bond strength and phase transformation energy barriers[61]. A higher compression modulus indicates that a larger force is needed to change the degree of atomic separation. Therefore, a low compression modulus generally implies a low shear modulus, which directly influences the dislocation behavior through the dislocation line tension[73]. The elevated compression moduli are associated with deeper interatomic potential wells, requiring significant energy barriers to be overcomed during compression. Conversely, the reduced compression moduli can diminish the resistance to dislocation motion, promoting dislocation glide and thereby enhancing ductility.

4.3. Microstructural mechanism for achieving striking comprehensive properties

4.3.1. Mechanical properties. In contrast to the as-deposited UHSDS, the as-tempered UHSDS mainly consists of the martensite laths together with nanoscale precipitates NiAl and ε-Cu, exhibiting striking comprehensive mechanical properties. To assess the mechanical contributions of strength of the lath martensite (σ_{mart}), solid-solution strengthening (σ_{sss}) and precipitate strengthening (σ_{pss})[74], the strengthening mechanism of the UHSDS is expressed by Equation (6):

$$\sigma_{YS} = \sigma_0 + \sigma_{mart} + \sigma_{sss} + \sigma_{ps} \tag{6}$$

where σ_{YS} represents the yield strength and σ_0(50 MPa) represents the lattice friction stress. The strength of the martensite matrix is attributed primarily to the augmented grain boundary area and dislocation density. The block size is defined as the effective grain size, the grain boundary strengthening is quantified via the Hall−Petch equation for d_{bolck}[75], and the strengthening induced by the increased dislocation density is described via the Taylor equation[76]. Therefore, the magnitude of the strength increment contributed by lath martensite is determined by Equation (7)[77]:

$$\sigma_{mart} = \frac{300}{\sqrt{d_{\text{bolck}}}} + \beta \mathrm{M} \mu b \sqrt{\rho} \tag{7}$$

where d_{bolck}(1.71 μm for the as-deposited UHSDS and 1.75 μm for the as-tempered UHSDS) can be obtained from the EBSD pattern (Figure 8), β (0.23) is a constant coefficient[78], and M (2.9 for BCC) represents the Taylor orientation factor. Additionally, b (0.249 nm) denotes the Burgers vector[41]. μ (71 GPa) corresponds to the matrix's shear modulus[79]. ρ is defined as the dislocation density, and based on the established relation $0.9\rho = \rho_{\text{GND}}$ (1.93×10^{15} m^{-2} for the as-deposited UHSDS and 1.86×10^{15} m^{-2} for the as-tempered UHSDS)[80], the value of ρ is calculated to be 2.14×10^{15} m^{-2} for the as-deposited UHSDS and 2.07×10^{15} m^{-2} for the as-tempered UHSDS.

Solid-solution strengthening (σ_{sss}) is evaluated via the Fleischer equation (Equation (8)), which quantifies the increase in critical resolved shear stress caused by substitutional solute atoms[81].

$$\sigma_{sss} = \sum_i (\beta_i x_i)^{1/2} \tag{8}$$

where x_i signifies the atomic fraction of i-th solute element, while β_i refers to the corresponding strengthening constant related to its lattice and modulus mismatch with Fe, as detailed in Table 8[81].

In accordance with the Orowan-Ashby mechanism[4], precipitation strengthening is quantified by Equation (9) as the additional stress necessary for dislocation bypass of fine precipitates:

$$\sigma_{ps} = 0.538 \frac{\mu b}{r_p} f_p^{1/2} \ln\left(\frac{f_p}{2b}\right) \tag{9}$$

where f_p (0.09% for the as-deposited sample and 2.48% for the as-tempered sample) signifies the volume fraction of the precipitates, and r_p (6.13 nm for the as-deposited sample and 3.56 nm for the as-tempered sample) corresponds to the mean radius of the precipitates. The values for f_p and r_p are statistical averages derived from 15 TEM images processed by the "Analyze Particles" feature in ImageJ. Specifically, f_p is calculated via Equation (10)[82]:

$$f_p = \frac{A_p}{A_f} \times 100\% \tag{10}$$

where A_p represents the overall area occupied by the precipitates, while A_f represents the area of the complete viewing field.

Figure 11(a) schematically illustrates the strengthening mechanism for the LDEDed UHSDS. The as-deposited UHSDS exhibits a combination of primarily martensitic strength (including grain boundary strengthening and dislocation strengthening), solid-solution strengthening from solute

Table 8. Solid solution constants for the different solute elements.

Element	Cr	Ni	Si	Al	Cu
β_i(MPa/at)	434	334	732	129	220

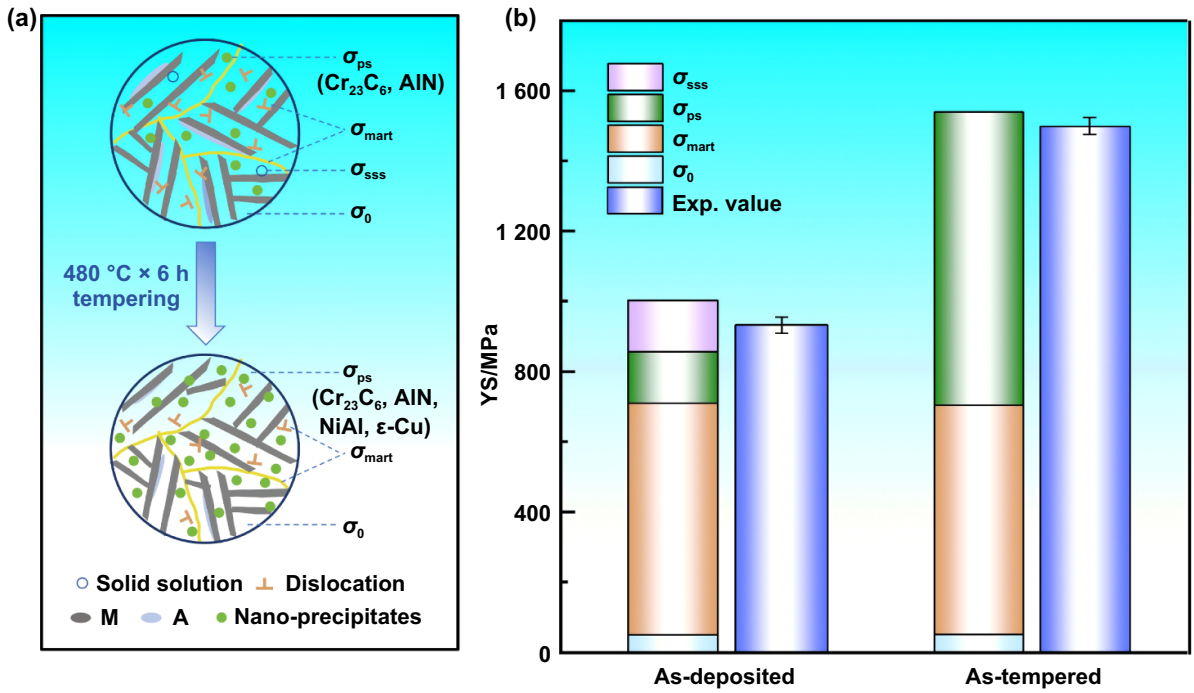

Figure 11. Strengthening mechanism and contribution analysis for UHSDS under different conditions. (a) Strengthening mechanisms, (b) strength contributions.

atoms, and moderate precipitate strengthening. In comparison, the as-tempered UHSDS is contributed by the dominant precipitate strengthening and martensitic matrix due to a much higher number density of nano-precipitates, accompanied by a slight reduction in dislocation density and essentially unchanged grain boundaries.

Based on the above analysis and quantitative evaluations, the individual strengthening contributions to the YS are clearly displayed in Figure 11(b). Specifically, the strength contribution values from σ_{sss}, σ_{mart} and σ_{ps} were calculated to be 173.4 MPa, 660.5 MPa, and 115.3 MPa, respectively, for the as-deposited UHSDS. In contrast, the corresponding contributions from σ_{mart} and σ_{ps} for the as-tempered UHSDS were determined as 649.1 MPa and 827.6 MPa, respectively. Therefore, the YS values of the as-deposited and as-tempered UHSDS are calculated via Equation (6) as 999.2 MPa and 1 526.7 MPa, respectively, which are in good agreement with the experimental average values of 934 MPa and 1 502 MPa, respectively (Figure 7(a)).

Noteworthily, the ductility of the as-tempered UHSDS doubled without compromising strength, which can be attributed to the following four main factors. (i) Transformation-induced plasticity (TRIP) effect. Reverted austenite, primarily located at martensite lath boundaries, can progressively transform into martensite during deformation. The resulted TRIP effect can dissipate energy and delay the onset of localized necking, significantly enhancing ductility[83]. (ii) Tempered martensite. The content of martensite increased from 75.7 vol% to 82.3 vol% after tempering treatment. The tempered martensite matrix can facilitate the uniform plastic deformation, synergistically enhancing ductility in combination with the reverted austenite[84]. (iii) Reduced dislocation density. A lower degree of dislocation accumulation can diminish the stress concentration and thereby has a beneficial effect on preventing crack initiation and improving ductility[85]. (iv) Reduced residual stress. After tempering heat treatment, the stress distribution was homogenized, and thus, the macroscopic ductility can be enhanced by enabling more coordinated deformation across all the regions. Meanwhile, the reduction of residual stress has been demonstrated to synergistically improve the plastic deformability of the material via crack suppression, microstructural softening and deformation homogenization[86].

4.3.2. Corrosion resistance. After a single-step tempering treatment, the LDEDed specimen exhibits enhanced mechanical properties simultaneously with improved corrosion resistance. This can be attributable to the inhibition of Cr depletion. On the one hand, a homogeneous Cr distribution network can be formed through Cu segregation at the core of the ε-Cu phases[87]. Herein, nano-sized ε-Cu phases can expel Cr atoms

from the surrounding matrix during the precipitation, thereby reducing Cr-depleted zones caused by carbide precipitation. This effectively reduces Cr depletion around grain boundaries or precipitated phases, thus lowering the local corrosion susceptibility. On the other hand, Cr consumption at grain boundaries can be reduced by the intragranular precipitation of nano-sized NiAl phases[88]. Nano-sized ε-Cu phases can effectively suppress the precipitation of coarse NiAl phases at grain boundaries while promoting the intragranular precipitation of nano-sized NiAl phases. As a consequence, the diffusion and loss of Cr to the grain boundaries was inhibited. The massive distribution of nanoscale ε-Cu phases and NiAl phases can also create multiple pinning points to obstruct the diffusion paths of Cr, thus preventing local fluctuations in the Cr concentration[89].

5. Conclusion

This work opens a new pathway for developing ultrahigh strength and ductility steels (UHSDS) by applying an interpretable PF-ML design approach. This strategy has dramatically accelerated the discovery process and enabled the introduction of a low-cost, short-process strategy for additively manufacturing UHSDS with exceptional corrosion resistance, thereby overcoming critical limitations in current additively manufactured steels. In this study, we successfully designed a novel cost-effective and corrosion-resistant Fe-15Cr-3.2Ni-0.8Mn-0.6Cu-0.56Si-0.4Al-0.16C UHSDS, achieving outstanding comprehensive properties after a 480 °C × 6 h single-step tempering treatment. Some critical findings have been obtained and are illustrated below:

(i) *PF-ML-guided alloy design concept.* The PF-ML strategy is highly effective in exploring the intricate relationships among the alloying elements, processing parameters, and target properties. Key insights derived from SHAP analyses reveal that elements such as Cr, Ni, Cu, and Al are crucial for synergistically enhancing the strength and ductility of UHSDS, guided by fundamental physical chemistry principles.

(ii) *Optimized microstructure via single-step tempering.* After the optimized single-step tempering heat treatment, the as-tempered UHSDS exhibits an extremely homogeneous microstructure dominated by lath martensite, along with retained austenite, reversed austenite, and nano-precipitates (AlN, NiAl, and ε-Cu), contributing to the exceptional properties of the UHSDS.

(iii) *Breakthrough comprehensive performance.* The designed UHSDS exhibits a striking strength−ductility combination, with a UTS of (1 713 ±17) MPa, a YS of (1 502 ± 33) MPa, and an EL of (15.5 ± 0.7)%. Meanwhile, the enhanced corrosion resistance was achieved dramatically, as evidenced by an exceptionally low corrosion rate of 0.105 mm·a^{-1}, which is much lower than that of AISI 420 stainless steel.

This study has demonstrated the effectiveness of the novel PF-ML design strategy in advancing the additive manufacturing of UHSDS components, achieving synergistic enhancements in both mechanical properties and corrosion resistance. This strategy is also applicable to other alloy systems for additive manufacturing.

Acknowledgments

This work was financially supported by the National Natural Science Foundation of China (No. 52375341).

ORCID iDs

Tao Zhu 0000-0002-5879-5980
Cunliang Pan 0000-0002-7559-6983
Xudong An 0009-0006-2825-0062
Hongmei Zhu 0000-0002-1944-4766

References

[1] Su J L, Li Q, Teng J, Ng F L, Shen Z L, Goh M H, Jiang F L, Sing S L, Yang T and Tan C L. 2025. Programmable mechanical properties of additively manufactured novel steel. *Int. J. Extrem. Manuf.* **7**, 015001.
[2] Tan C L, Weng F, Sui S, Chew Y and Bi G J. 2021. Progress and perspectives in laser additive manufacturing of key aeroengine materials. *Int. J. Mach. Tools Manuf.* **170**, 103804.
[3] Su J L, Chen L Q, Van Petegem S, Jiang F L, Li Q Z, Luan J H, Sing S L, Wang J and Tan C L. 2025. Additive manufacturing metallurgy guided machine learning design of versatile alloys. *Mater. Today* **88**, 240–250.
[4] Zhu H M, Ouyang M N, Hu J P, Zhang J W and Qiu C J. 2021. Design and development of TiC-reinforced 410 martensitic stainless steel coatings fabricated by laser cladding. *Ceram. Int.* **47**, 12505–12513.
[5] Kürnsteiner P, Wilms M B, Weisheit A, Gault B, Jägle E A and Raabe D. 2020. High-strength Damascus steel by additive manufacturing. *Nature* **582**, 515–519.
[6] Zheng Y S, Liu F G, Gao J Y, Liu F C, Huang C P, Zheng H Z, Wang P F and Qiu H. 2023. Effect of different heat input on the microstructure and mechanical properties of laser cladding repaired 300M steel. *J. Mater. Res. Technol.* **22**, 556–568.
[7] Ran X Z, Liu D, Tang H B, Wang H M, Santucci R J and Scully J R. 2021. Hydrogen diffusion and trapping in laser additively manufactured ultra-high strength AerMet100 steel. *Corrosion* **77**, 1043–1059.
[8] Wang M, Wang Q, Lin X and Huang W D. 2019. Microstructure and mechanical properties of laser solid formed 30Cr–Mn–Si–Ni–2A ultra-high-strength steel. *Sci. Technol. Weld. Join* **24**, 457–464.
[9] Tian Y, Chadha K and Aranas C. 2021. Laser powder bed fusion of ultra-high-strength 420 stainless steel: microstructure characterization, texture evolution and mechanical properties. *Mater. Sci. Eng. A* **805**, 140790.
[10] Zhang Y J et al. 2025. Machine learning enhanced metal 3D printing: high throughput optimization and material transfer extensibility. *Int. J. Extrem. Manuf.* **7**, 045004.
[11] Tan Y M, Wang X W, Kang Z T, Ye F, Chen Y F, Zhou D W, Zhang X C and Gong J M. 2022. Creep lifetime prediction of 9% Cr martensitic heat-resistant steel based on ensemble learning method. *J. Mater. Res. Technol.* **21**, 4745–4760.

[12] Shen C G, Wang C C, Wei X L, Li Y, van der Zwaag S and Xu W. 2019. Physical metallurgy-guided machine learning and artificial intelligent design of ultrahigh-strength stainless steel. *Acta Mater.* **179**, 201–214.
[13] He X, Gao X H, Shi Z X, Song L Y, Li J B and Du L X. 2023. Study on properties prediction and reverse design of weathering steel based on machine learning and multi-objective optimization. *J. Plast. Eng.* **30**, 167–177.
[14] Cui C Y, Cao G M, Li X, Gao Z W, Liu J J and Liu Z Y. 2023. A strategy combining machine learning and physical metallurgical principles to predict mechanical properties for hot rolled Ti micro-alloyed steels. *J. Mater. Process. Technol.* **311**, 117810.
[15] Tan C L et al. 2023. Machine learning customized novel material for energy-efficient 4D printing. *Adv. Sci.* **10**, 2206607.
[16] Li X C, Zheng M J, Pan H, Mao C L and Ding W Y. 2024. An integrated design of novel RAFM steels with targeted microstructures and tensile properties using machine learning and CALPHAD. *J. Mater. Inf.* **4**, 27.
[17] Ouyang R H, Curtarolo S, Ahmetcik E, Scheffler M and Ghiringhelli L M. 2018. SISSO: a compressed-sensing method for identifying the best low-dimensional descriptor in an immensity of offered candidates. *Phys. Rev. Mater.* **2**, 083802.
[18] Zhang H T, Fu H D, He X Q, Wang C S, Jiang L, Chen L Q and Xie J X. 2020. Dramatically enhanced combination of ultimate tensile strength and electric conductivity of alloys via machine learning screening. *Acta Mater.* **200**, 803–810.
[19] Jiang L, Fu H D, Zhang Z H, Zhang H T, Zhang X B, Feng X M, Xu X Y, Mao M H and Xie J X. 2024. Synchronously enhancing the strength, toughness, and stress corrosion resistance of high-end aluminum alloys via interpretable machine learning. *Acta Mater.* **270**, 119873.
[20] Zhang Y, Xin S W, Zhou W, Wang X, Xu Y Y and Su Y J. 2025. A multi-objective feature optimization strategy for developing high-entropy alloys with optimal strength and ductility. *Mater. Genome Eng. Adv.* **3**, e70000.
[21] Liu Y T, Su J L, Li Y H, Han R, Wong R C W, Hui J H P and Sing S L. 2025. In-situ alloying modulation in additive manufacturing of titanium-tantalum alloy: from melt pool modelling to process development. *Mater. Sci. Eng. R* **166**, 101082.
[22] Dharmadhikari S, Menon N and Basak A. 2023. A reinforcement learning approach for process parameter optimization in additive manufacturing. *Addit. Manuf.* **71**, 103556.
[23] Su J L, Mo Y, Shangguan P J, Panwisawas C, Jiang F L and Sing S L. 2025. Additive manufacturing-by-design for support structures: a critical review. *Int. J. Extrem. Manuf.* **7**, 052002.
[24] Xue T J, Wallin T J, Menguc Y, Adriaenssens S and Chiaramonte M. 2020. Machine learning generative models for automatic design of multi-material 3D printed composite solids. *Extreme Mech. Lett.* **41**, 100992.
[25] Lundberg S M and Lee S I. 2017. A unified approach to interpreting model predictions. *In Proceedings of the 31st International Conference on Neural Information Processing Systems* (Curran Associates Inc., Long Beach, California, USA) pp 4768–4777.
[26] Alabrah A. 2023. An improved CCF detector to handle the problem of class imbalance with outlier normalization using IQR method. *Sensors* **23**, 4406.
[27] Schnitzer R, Schober M, Zinner S and Leitner H. 2010. Effect of Cu on the evolution of precipitation in an Fe–Cr–Ni–Al–Ti maraging steel. *Acta Mater.* **58**, 3733–3741.
[28] Akbari P, Zamani M and Mostafaei A. 2024. Machine learning prediction of mechanical properties in metal additive manufacturing. *Addit. Manuf.* **91**, 104320.
[29] Grbčić L et al. 2022. Coastal water quality prediction based on machine learning with feature interpretation and spatio-temporal analysis. *Environ. Model. Softw.* **155**, 105458.
[30] Chen T Q and Guestrin C 2016. XGBoost: a scalable tree boosting system. *In Proceedings of the 22nd ACM SIGKDD International Conference on Knowledge Discovery and Data Mining* (ACM, San Francisco, California, USA) pp 785–794.
[31] Saidi R, Bouaguel W and Essoussi N. 2018. Hybrid feature selection method based on the genetic algorithm and Pearson correlation coefficient. *Machine Learning Paradigms: Theory and Application* ed Hassanien A E. (Springer, Cham) pp 3–24.
[32] De Myttenaere A, Golden B, Le Grand B and Rossi F. 2016. Mean absolute percentage error for regression models. *Neurocomputing* **192**, 38–48.
[33] Gu Q H, Wang R, Xie H Y, Li X X, Jiang S and Xiong N X. 2021. Modified non-dominated sorting genetic algorithm III with fine final level selection. *Appl. Intell.* **51**, 4236–4269.
[34] Li B C, Zhu H M, Qiu C J and Zhang D K. 2020. Development of high strength and ductile martensitic stainless steel coatings with Nb addition fabricated by laser cladding. *J. Alloys Compd.* **832**, 154985.
[35] Li B C, Zhu H M, Qiu C J and Gong X K. 2019. Laser cladding and in-situ nitriding of martensitic stainless steel coating with striking performance. *Mater. Lett.* **259**, 126829.
[36] He X and Oyadiji S O. 2001. Application of coefficient of variation in reliability-based mechanical design and manufacture. *J. Mater. Process. Technol.* **119**, 374–378.
[37] Huang J X, Ando D and Sutou Y J. 2024. Heat-resistant aluminum alloy design using explainable machine learning. *Mater. Des.* **243**, 113057.
[38] Cheng H, He Z P, Ge M L, Che L, Zheng K Y, Si T Y and Zhao F. 2024. Composition design and optimization of Fe–C–Mn–Al steel based on machine learning. *Phys. Chem. Chem. Phys.* **26**, 8219–8227.
[39] Tang J F, Wang H D and Xiong L. 2023. Surrogate-assisted multi-objective optimization via knee-oriented Pareto front estimation. *Swarm Evol. Comput.* **77**, 101252.
[40] Pan C F, Lin W W, Zhou J X, Jian W, Chan K C, Chan Y L and Ren L. 2025. Novel machine learning driven design strategy for high strength Zn Alloys optimization with multiple constraints. *npj Comput. Mater.* **11**, 169.
[41] Tan C L, Chew Y X, Weng F, Sui S, Du Z L, Ng F L and Bi G J. 2021. Superior strength-ductility in laser aided additive manufactured high-strength steel by combination of intrinsic tempering and heat treatment. *Virtual Phys. Prototype* **16**, 460–480.
[42] Strakosova A, Kubásek J, Michalcová A, Průša F, Vojtěch D and Dvorský D. 2019. High strength X3NiCoMoTi 18-9-5 maraging steel prepared by selective laser melting from atomized powder. *Materials* **12**, 4174.
[43] Lek Y Z, Wang C C, Shen X J, Chen Z, Ramamurty U and Zhou K. 2022. Additive manufacturing of corrosion-resistant maraging steel M789 by directed energy deposition. *Mater. Sci. Eng. A* **857**, 144032.
[44] LeBrun T, Nakamoto T, Horikawa K and Kobayashi H. 2015. Effect of retained austenite on subsequent thermal processing and resultant mechanical properties of selective laser melted 17-4 PH stainless steel. *Mater. Des.* **81**, 44–53.
[45] Im H J, Ryou K, Kang T H, Jimbo S, Nambu S, Han J and Choi P P. 2023. Thermally driven changes in the microstructure and mechanical properties of martensitic 15-5 precipitation-hardened stainless steel during directed energy deposition. *Addit. Manuf.* **74**, 103729.
[46] Jiang C M, Ho J R, Tung P C and Lin C K. 2023. Tempering effect on the anisotropic mechanical properties of selective laser melted 420 stainless steel. *J. Mater. Eng. Perform* **32**, 5082–5096.
[47] Guo W F, Guo C and Zhu Q. 2018. Heat treatment behavior of the 18Ni300 maraging steel additively manufactured by selective laser melting. *Mater. Sci. Forum.* **941**, 2160–2166.

[48] Wang X P, Li W T, Yao Y J, Fan L Y, Wang J H, Wang W Y, Wen P Y, Yang Z G and Chen H. 2023. In-situ alloyed ultrahigh strength steels via additive manufacturing. *Addit. Manuf.* **77**, 103825.
[49] Asala G, Ola O T and Ojo O A. 2023. Effects of process variables on the quality and mechanical properties of 18%Ni-M350 maraging steel produced by direct energy deposition laser additive manufacturing. *Mater. Sci. Eng. A* **866**, 144646.
[50] Dong Y A, Lan X Q, Yang S Q, Lu J X, Yan S Y, Wei K W and Wang Z M. 2024. Effect of quenching and tempering treatments on microstructure and mechanical properties of 300M ultra-high strength steel fabricated by laser powder bed fusion. *Mater. Charact.* **212**, 113935.
[51] Saeidi N, Ashrafizadeh F and Niroumand B. 2014. Development of a new ultrafine grained dual phase steel and examination of the effect of grain size on tensile deformation behavior. *Mater. Sci. Eng. A* **599**, 145–149.
[52] Asadi M, De Cooman B C and Palkowski H. 2012. Influence of martensite volume fraction and cooling rate on the properties of thermomechanically processed dual phase steel. *Mater. Sci. Eng. A* **538**, 42–52.
[53] Xu T Z, Zhang S, Du Y, Wu C L, Zhang C H, Sun X Y, Chen H T and Chen J. 2024. Development and characterization of a novel maraging steel fabricated by laser additive manufacturing. *Mater. Sci. Eng. A* **891**, 145975.
[54] Li X F, Zhang J, Wang Y F, Shen S C and Song X L. 2016. Effect of hydrogen on tensile properties and fracture behavior of PH 13-8 Mo steel. *Mater. Des.* **108**, 608–617.
[55] Snir Y, Haroush S, Dannon A, Landau A, Eliezer D and Gelbstein Y. 2019. Aging condition and trapped hydrogen effects on the mechanical behavior of a precipitation hardened martensitic stainless steel. *J. Alloys Compd.* **805**, 509–516.
[56] Wang S Q, Zhao T L, Liu Z Y, Du C W and Li X G. 2021. Exploration of the processing scheme of a novel Ni(Fe, Al)-maraging steel. *J. Mater. Res. Technol.* **10**, 225–239.
[57] Pan M M, Zhang J and Zhang X M. 2022. Effect of Cu addition on phase fraction, mechanical properties and corrosion properties of Fe–Cr–Mn–Al duplex stainless steel. *Mater. Sci. Eng. A* **857**, 144095.
[58] Chen H J, Hsiao P C, Chien H K C, Lin K F, Chuo Y T, Huang C Y and Lin H C. 2025. Effects of heat treatment on microstructure, mechanical properties and corrosion resistance 13Cr-2Ni-2Mo martensitic stainless steel. *Mater. Charact.* **223**, 114909.
[59] Bommersbach P, Alemany-Dumont C, Millet J P and Normand B. 2005. Formation and behaviour study of an environment-friendly corrosion inhibitor by electrochemical methods. *Electrochim. Acta* **51**, 1076–1084.
[60] Wu W, Qin L Z, Cheng X Q, Xu F F and Li X G. 2023. Microstructural evolution and its effect on corrosion behavior and mechanism of an austenite-based low-density steel during aging. *Corros. Sci.* **212**, 110936.
[61] Lide D R and Frederikse H P R. 1997. *CRC Handbook of Chemistry and Physics* 78th edn. (CRC Press, Boca Raton).
[62] Sanditov D S, Mashanov A A and Darmaev M D. 2009. Propagation velocity of longitudinal and transverse acoustic waves and anharmonicity of lattice oscillations. *Tech. Phys.* **54**, 1398–1401.
[63] Radjai M and Bouhemadou A. 2023. Physical properties of $BaRu_2X_2$ (X= P, As) superconducting compound sunder pressure effects: ab initio study. *Physica C* **604**, 1354176.
[64] Shang S L, Zhou B C, Wang W Y, Ross A J, Liu X L, Hu Y J, Fang H Z, Wang Y and Liu Z K. 2016. A comprehensive first-principles study of pure elements: vacancy formation and migration energies and self-diffusion coefficients. *Acta Mater.* **109**, 128–141.
[65] Rao W F and Khachaturyan A G. 2011. Phase field theory of proper displacive phase transformations: structural anisotropy and directional flexibility, a vector model, and the transformation kinetics. *Acta Mater.* **59**, 4494–4503.
[66] Li J P, Jiang W G, Zhang Y, Liu L Y, Yu Y Z, Luan J H, Jiao Z B, Liu C T and Zhang Z W. 2024. Evolution and strengthening of nanoprecipitates in a high strength maraging stainless steel. *Mater. Sci. Eng. A* **915**, 147198.
[67] Li S H, Tong Z, Zhang X Y and Bao H. 2020. Thermal conductivity and Lorenz ratio of metals at intermediate temperatures with mode-level first-principles analysis. *Phys. Rev. B* **102**, 174306.
[68] Klemens P G. 1959. Deviation from Matthiessen's rule and lattice thermal conductivity of alloys. *Aust. J. Phys.* **12**, 199–203.
[69] Lu H, Huang X C, Hou R F and Li D Y. 2018. Understanding the effect of Ni on mechanical and wear properties of low-carbon steel from a view-point of electron work function. *Metall. Mater. Trans. A* **49**, 2612–2621.
[70] Nam S, Lee C G, Jang T J, Sung M Y, Kim S H, Park E S and Sohn S S. 2025. Enhanced strength-ductility synergy in $L1_2$-strengthened high-entropy alloys via precipitation-induced matrix thermodynamic tailoring. *Mater. Char.* **230**, 115724.
[71] Kahn A. 2016. Fermi level, work function and vacuum level. *Mater. Horiz.* **3**, 7–10.
[72] Kadowaki M, Saengdeejing A, Muto I, Chen Y, Doi T, Kawano K, Sugawara Y and Hara N. 2021. First-principles investigation on work function of martensitic carbon steels: effect of interstitial carbon on anodic dissolution resistance. *J. Electrochem. Soc.* **168**, 111503.
[73] Siddique S, Ahmad S, Zeba I, Gulzar F, Shakil M and Gillani S S A. 2023. Static isotropic pressure induced semiconductor–metal transition and its impact on structural, electronic, elastic, mechanical and optical properties of $SrCeO_3$. *Eur. Phys. J. Plus* **138**, 844.
[74] Wang D, Yang S G, Jiang H, Cao K, Xiao J, Guo H, Liu R Q and Zhao A M. 2024. Study on the relationship between the refined hierarchical microstructure, yield strength and impact toughness of low-carbon martensitic steel at different quenching temperatures. *Mater. Sci. Eng. A* **896**, 146271.
[75] Morito S, Yoshida H, Maki T and Huang X. 2006. Effect of block size on the strength of lath martensite in low carbon steels. *Mater. Sci. Eng. A* **438–440**, 237–240.
[76] Li J P, Jiang W G, Zhang Y, Liu L Y, Yu Y Z, Luan J H, Jiao Z B, Liu C T and Zhang Z W. 2025. Formation of core-shell nanoprecipitates and their effects on work hardening in an ultrahigh-strength stainless steel. *Int. J. Plast.* **184**, 104184.
[77] Li J P, Zhang Y, Jiang W G, Luan J H, Jiao Z B, Liu C T and Zhang Z W. 2025. Enhancing work hardening through tuning TRIP by nano-precipitates in maraging stainless steels. *Int. J. Plast.* **186**, 104265.
[78] Gao G H, Gao B, Gui X L, Hu J, He J Z, Tan Z L and Bai B Z. 2019. Correlation between microstructure and yield strength of as-quenched and Q&P steels with different carbon content (0.06-0.42 wt%C). *Mater. Sci. Eng. A* **753**, 1–10.
[79] Wei X H, Cao X, Luan J H, Jiao Z B, Liu C T and Zhang Z W. 2022. Synergy of strengthening and toughening of a Cu-rich precipitate-strengthened steel. *Mater. Sci. Eng. A* **832**, 142487.
[80] Smith T R, Sugar J D, San Marchi C and Schoenung J M. 2019. Strengthening mechanisms in directed energy deposited austenitic stainless steel. *Acta Mater.* **164**, 728–740.
[81] Galindo-Nava E I and Rivera-díaz-del-castillo P E J. 2015. A model for the microstructure behaviour and strength evolution in lath martensite. *Acta Mater.* **98**, 81–93.
[82] Callister J W D and Rethwisch D G. 2020. *Materials Science and Engineering: An Introduction* 10th edn. (Wiley Press, Hoboken).

[83] Tan L H, Li D D, Yan L C, Pang X L and Gao K W. 2023. Simultaneous enhancement of strength-ductility via multiple precipitates and austenite in a novel precipitation-hardened martensitic stainless steel. *Mater. Sci. Eng. A* **873**, 145062.

[84] Kan C L, Zhao L, Cao Y, Ma C Y, Peng Y and Tian Z L. 2024. Microstructure evolution and strengthening behavior of maraging steel fabricated by wire arc additive manufacturing at different heat treatment processes. *Mater. Sci. Eng. A* **909**, 146804.

[85] Zhang Y P, Zhan D P, Qi X W and Jiang Z H. 2018. Austenite and precipitation in secondary-hardening ultra-high-strength stainless steel. *Mater. Charact.* **144**, 393–399.

[86] Prakash P, Midawi A, Muhammad W, Wells M and Hadadzadeh A. 2024. Role of heat treatment conditions in the high-temperature deformation behavior of laser-powder bed fused Fe–Cr–Ni–Al maraging stainless steel. *Mater. Sci. Eng. A* **909**, 146837.

[87] Fabian R and Hadadzadeh A. 2023. Breaking strength-ductility trade-off in laser-powder bed fused Fe–Cr–Ni–Al maraging stainless steel: controlled precipitation and preserved dislocations. *Mater. Sci. Eng. A* **868**, 144761.

[88] Yang B B, Song Y Y, Hao L, Jiang H C and Rong L J. 2024. Microstructure and corrosion resistance of low-carbon martensitic stainless steel 0Cr13Ni4Mo with 3% Cu addition. *Acta Metall. Sin.* **60**, 1656–1666.

[89] Yang X C, Di X J, Wang J S, Fang C, Fu W, Ba L Z, Zhou X F, Zhang C Y and Li C N. 2023. The co-precipitation evolution of NiAl and Cu nanoparticles and its influence on strengthening and toughening mechanisms in low-carbon ultra-high strength martensite seamless tube steel. *Int. J. Plast.* **166**, 103654.